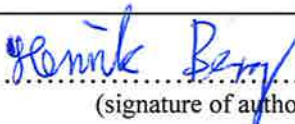




Universitetet  
i Stavanger

FACULTY OF SCIENCE AND TECHNOLOGY

## MASTER'S THESIS

Study programme/specialization: Petroleum Engineering Natural Gas Technology	Spring semester, 2018  Open
Author: Henrik Berg	 ..... (signature of author)
Programme coordinator:  Prof. Zhixin Yu  Supervisor:  Prof. Zhixin Yu	
Title of master's thesis:  The promotional effect of Ca, Mg and Rh on the activity of Ni-based catalyst from hydrotalcite precursor for dry reforming of methane	
Credits (ECTS): 30	
Keywords: Dry reforming of methane Hydrotalcite derived catalysts Catalyst preparation Noble metal addition Catalyst characterization Catalyst deactivation	Number of pages: 54  Stavanger, 15.06.2018

## **Acknowledgement**

I would like to thank my supervisor Professor Zhixin Yu for the opportunity to write this thesis, and the University of Stavanger (UiS) that allowed me to use their labs for the different experiments in my thesis. I would also like to thank the Ph.d candidates Dori Kalai and Kristian Stangeland, and my fellow student Huynh Lan Huong, which gave a lot of help and support to my Master thesis.

My educational background before starting the Master in petroleum engineering was a bachelor in Mathematics and Physics, with only a brief course in chemistry, and the necessary petroleum courses needed to apply for a Master in petroleum engineering. Therefore, my knowledge of chemical engineering was very limited. This made the experiments challenging to execute, with a "learn as you perform" methodology. However, this also made it very interesting and fun to do the various experiments.

The reason I chose the specialization in natural gas technology is that I have always been interested in what natural gas can be utilized for on a commercial level. It was when I took the course Natural Gas Conversion by Professor Zhixin Yu in the autumn semester of 2017 that I was presented for the process of dry reforming of methane. When a thesis on this subject became available, I did not hesitate to apply for it since it was exactly what I wanted to write about.

Finally, I would like to thank my family for their support throughout my studies.

## Abstract

The world strives towards a way to decrease CH<sub>4</sub> and CO<sub>2</sub> emissions to the atmosphere. A way to do this is to utilize these gases in processes that can make useful products. One of these are dry reforming of methane (DRM), where CH<sub>4</sub> and CO<sub>2</sub> are used to produce syngas with a H<sub>2</sub>/CO ratio of approximately 1.

The goal of this thesis was to prepare six catalysts derived from hydrotalcite (HT) precursors, similar to hydrotalcites (HTs) with alkaline earth or noble metal promoters and use them in the DRM reaction while studying their activity, selectivity and stability. Four HT catalysts with calcium (Ca) and magnesium (Mg) as promoters were prepared with the coprecipitation method. In addition, two catalysts were prepared by adding rhodium (Rh) to the Mg catalysts with the incipient wetness method utilising the memory effect of HTs. The catalysts were characterized by N<sub>2</sub> adsorption/desorption, temperature programmed reduction (TPR), temperature programmed desorption (TPD), H<sub>2</sub>-chemisorption and X-ray diffraction (XRD) measurements. The catalysts were studied in a DRM reaction at 750°C and 1 bar for 15 h time on stream (TOS). The reaction was run over 200 ml/min CH<sub>4</sub>/CO<sub>2</sub> 1:1 ratio, giving a gas hourly space velocity of 240000  $\frac{ml}{g_{cat}\cdot h}$ . The NiMgAl catalysts had high initial activities but experienced a rapid decrease in CH<sub>4</sub> and CO<sub>2</sub> conversions. The most stable catalysts were the NiMgAlRh catalysts, that showed good stability for CH<sub>4</sub> and CO<sub>2</sub> conversions with very little deactivation, due to the noble metal addition. The NiCaAl catalysts also demonstrated stable activity, ascribed to the CO<sub>2</sub> adsorption capacity of Ca, which could gasify deposited carbon.

# Contents

<b>Acknowledgement</b>	<b>ii</b>
<b>Abstract</b>	<b>iii</b>
<b>List of Figures</b>	<b>vi</b>
<b>List of Tables</b>	<b>vii</b>
<b>1 Introduction</b>	<b>1</b>
<b>2 Literature review</b>	<b>2</b>
2.1 Syngas production from methane . . . . .	2
2.1.1 Steam reforming of methane (SRM) . . . . .	2
2.1.2 Partial oxidation (POX) . . . . .	3
2.1.3 Autothermal reforming (ATR) . . . . .	4
2.2 Dry reforming of methane (DRM) . . . . .	5
2.2.1 Side reactions . . . . .	5
2.2.2 Kinetic models . . . . .	6
2.2.3 Deactivation of catalyst . . . . .	8
2.3 Hydrotalcite derived catalysts . . . . .	9
2.4 Theoretical background for the experiments . . . . .	11
2.4.1 Co-precipitation and Incipient Wetness impregnation . . . . .	11
2.4.2 Calcination . . . . .	11
2.4.3 Specific surface area, pore volume and pore size distribution . . . . .	12
2.4.3.1 N <sub>2</sub> adsorption/desorption procedure . . . . .	12
2.4.3.2 BET surface area . . . . .	14
2.4.3.3 BJH pore volume and size . . . . .	15
2.4.4 Crystallography and X-ray Diffraction (XRD) . . . . .	15
2.4.4.1 Diffraction and Bragg's law . . . . .	15
2.4.4.2 X-ray Powder Diffraction and Scherrer equation . . . . .	16
2.4.5 Chemisorption . . . . .	17
2.4.6 Temperature Programmed Reduction/Desorption (TPR/TPD) . . . . .	18
<b>3 Experimental work</b>	<b>20</b>
3.1 Catalyst preparation . . . . .	20
3.2 Catalyst characterization . . . . .	23
<b>4 Results and discussion</b>	<b>25</b>
4.1 X-ray diffraction . . . . .	25
4.2 N <sub>2</sub> Physisorption . . . . .	26

4.3	TPR . . . . .	31
4.4	TPD . . . . .	32
4.5	H <sub>2</sub> -chemisorption . . . . .	33
4.6	DRM reaction . . . . .	33
4.7	XRD pattern of the catalysts after DRM reaction . . . . .	37
<b>5</b>	<b>Conclusion</b>	<b>38</b>
<b>A</b>	<b>Calculations used in the thesis</b>	<b>43</b>
A.1	Summary of precursor calculation . . . . .	43
A.2	Addition of rhodium to 20NiMgAl catalyst . . . . .	45
<b>B</b>	<b>Calculation of mass for TPR experiment based on the sensitivity and resolution factor</b>	<b>46</b>

## List of Figures

Figure 1: Conversion processes for methane at high and low temperatures [4] . . . .	page 2
Figure 2: Flowsheet for the SRM process [5] . . . . .	page 3
Figure 3: ATR reactor diagram [7] . . . . .	page 4
Figure 4: The general build-up structure of hydrotalcites . . . . .	page 10
Figure 5: Adsorption isotherms from N <sub>2</sub> adsorption [28] . . . . .	page 12
Figure 6: The six hysteresis shapes from the N <sub>2</sub> adsorption/desorption isotherm [29]	page 13
Figure 7: Diffraction of two X-ray beams . . . . .	page 16
Figure 8: Simplified schematic representation of the TPR/TPD instrument [36] .	page 18
Figure 9: Set-up of the aging process . . . . .	page 21
Figure 10: Set-up of the calcination process . . . . .	page 22
Figure 11: DRM reaction schematic . . . . .	page 24
Figure 12: XRD diffraction pattern of HT precursors . . . . .	page 25
Figure 13: XRD diffraction pattern of the as-prepared rhodium precursors . . . .	page 25
Figure 14: XRD diffraction patterns of calcined catalysts . . . . .	page 26
Figure 15: Nitrogen adsorption/desorption isotherms for the precursors . . . . .	page 27
Figure 16: Pore size distribution for the precursors . . . . .	page 28
Figure 17: Pore size distribution for the NiCaAl precursors . . . . .	page 29
Figure 18: Nitrogen adsorption/desorption isotherms for calcined catalysts . . . .	page 29
Figure 19: Pore size distribution for calcined catalysts . . . . .	page 30
Figure 20: Pore size distribution for calcined NiCaAl catalysts . . . . .	page 31
Figure 21: TPR of the catalysts . . . . .	page 32
Figure 22: TPD of the catalysts . . . . .	page 33
Figure 23: CH <sub>4</sub> conversion for DRM reaction at 750°C and 1 bar . . . . .	page 34
Figure 24: CO <sub>2</sub> conversion for DRM reaction at 750°C and 1 bar . . . . .	page 34
Figure 25: H <sub>2</sub> /CO conversion for DRM reaction at 750°C and 1 bar . . . . .	page 35
Figure 26: XRD profile of spent catalysts after DRM reaction. . . . .	page 37

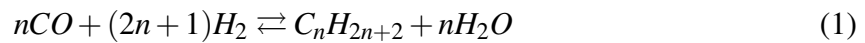
## List of Tables

Table 1: Reactions in a DRM process .....	page 8
Table 2: Denotation and metal content (wt %) of the catalysts .....	page 20
Table 3: Summary of catalyst preparation processes .....	page 22
Table 4: Summary of N <sub>2</sub> Physisorption for the HT precursors .....	page 27
Table 5: NiMgAlRh catalysts (precursors and calcined) compared with calcined 20NiMgAl catalyst .....	page 28
Table 6: Summary of N <sub>2</sub> Physisorption for the calcined catalysts .....	page 30
Table 7: Results from H <sub>2</sub> chemisorption of the catalysts .....	page 33
Table 8: Results from the DRM reaction .....	page 35
Table 9: CH <sub>4</sub> and CO <sub>2</sub> deactivation from the DRM reaction .....	page 35
Table 10: Initial moles from mass calculation for Mg catalysts .....	page 43
Table 11: Initial moles from mass calculation for Ca catalysts .....	page 44
Table 12: Moles for mass calculation of Mg catalysts .....	page 44
Table 13: Moles for mass calculation of Ca catalysts .....	page 44
Table 14: Mass of the salts used for co-precipitation of Mg catalysts .....	page 44
Table 15: Mass of the salts used for co-precipitation of Ca catalysts .....	page 44
Table 16: Summary of IW method for the prepared Rh catalysts .....	page 45
Table 17: Moles of cations for the Mg catalysts .....	page 46
Table 18: Moles of cations for the Ca catalysts .....	page 46
Table 19: Molar mass of oxides .....	page 46
Table 20: Summary of calculations for <i>K</i> and <i>P</i> .....	page 47

# 1 Introduction

Dry reforming of methane (DRM) was first investigated by Fischer and Tropsch in 1928, with nickel (Ni) and carbon monoxide (CO) as catalysts. [1] Since then technology has developed a lot further, and today DRM has gotten new attention as a way to utilize two of the gases that do a lot of damage to our environment: carbon dioxide (CO<sub>2</sub>) and methane (CH<sub>4</sub>). Every year the concentration of CO<sub>2</sub> in the atmosphere increases, which have a large impact on global warming of our planet. Both CO<sub>2</sub> and CH<sub>4</sub> are greenhouse gases, although there are much less CH<sub>4</sub> than CO<sub>2</sub> in the atmosphere. However, one mole of CH<sub>4</sub> is 24 times more effective at absorbing infrared radiation than one mole of CO<sub>2</sub>. Given in mass measurement, 1 kg of CH<sub>4</sub> is 66 times more effective as a greenhouse gas than 1 kg of CO<sub>2</sub>. In addition, combustion of methane can produce carbon dioxide and thereby increase the CO<sub>2</sub> content in the atmosphere. [2]

A way to reduce CO<sub>2</sub> and CH<sub>4</sub> emissions to the atmosphere is the process of dry reforming of methane (DRM), which utilizes both of these components to produce more useful products that can be used in the industry, e.g. in the Fischer-Tropsch (F-T) process (Eq. 1). In this process the ratio of hydrogen and carbon monoxide (H<sub>2</sub>/CO ratio) that is needed is 2:1. [1] [3]



To reduce the energy needed for the DRM reaction, different types of catalysts has been tested in the reaction process. In recent years there has been an increased interest in using hydrotalcite with different types of promoters as a catalyst for this reaction. But DRM is not considered as a usable commercial process yet, because carbon formation from the reaction will occur and thereby cause deactivation of the catalyst. Also, since it is a highly endothermic reaction high temperature will be needed, so the catalyst can also be exposed to thermal sintering.



## 2 Literature review

### 2.1 Syngas production from methane

There are different technological processes existing today that uses methane to make syngas. This will become more important in the future as the world now is changing to explore and develop natural gas from unconventional reserves like shale gas, and to reduce the dependence on crude oil resources. This is the result of the new fracturing technology that makes shale gas easier and cheaper to produce than before. There are a number of industrial pathways to convert methane to make desired products such as fuel and chemicals. Figure 1 shows the main methane conversion processes that are interesting to develop further today. [4] In this thesis partial oxidation, steam reforming and autothermal reforming will only be given a brief overview, while the main focus is on dry reforming of methane.

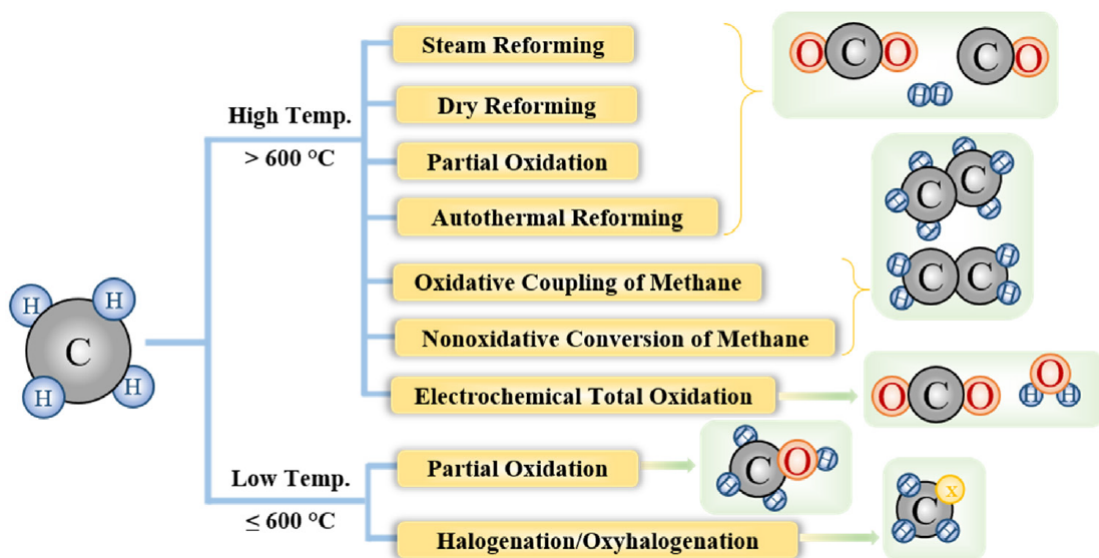


Figure 1: Conversion processes for methane at high and low temperatures [4]

#### 2.1.1 Steam reforming of methane (SRM)

Hydrogen has been produced from SRM reaction for decades. Figure 2 shows a flowsheet for the SRM process.

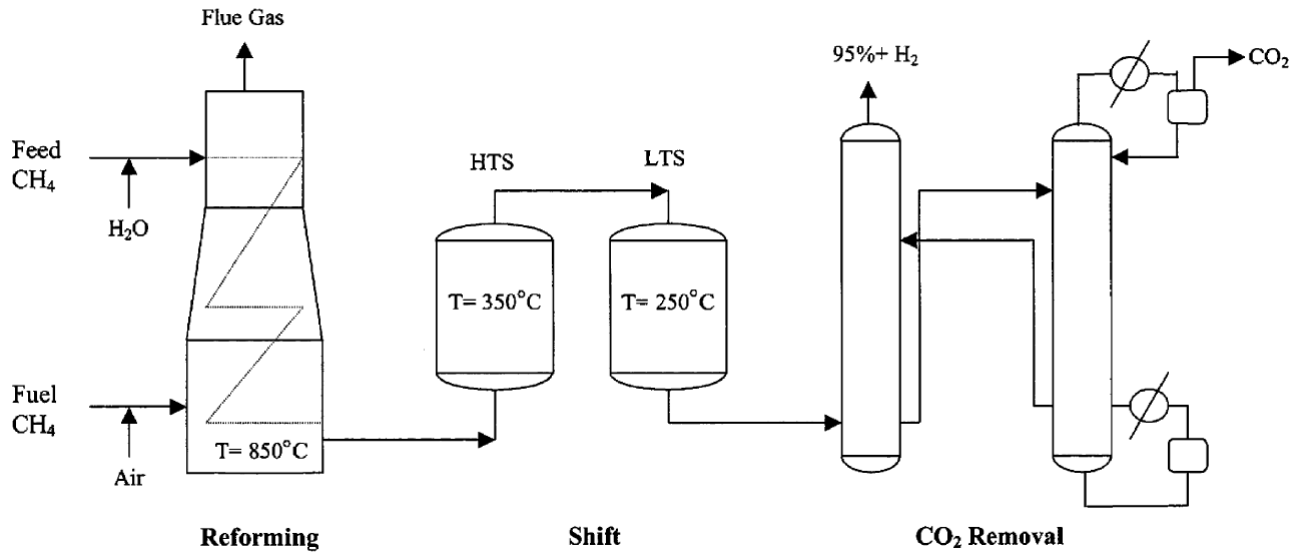
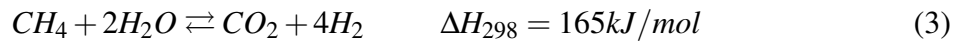
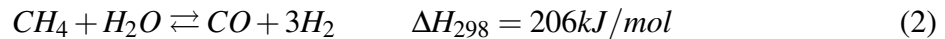
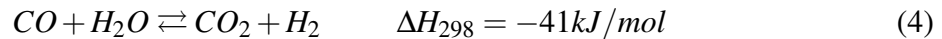


Figure 2: Flowsheet for the SRM process [5]

The process consists of three reactions where methane reacts with steam fed into the furnace. Hydrogen and carbon dioxide is formed in an endothermic process.

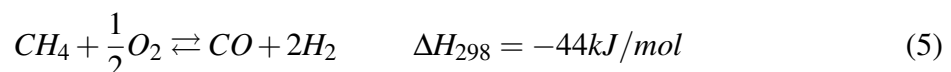


The temperature and pressure for the reaction are 800-1000°C and 14-20 atm over a nickel-based catalyst. Natural gas is added in the furnace as a supplement to provide the heat needed for the endothermic reaction. The products are then led to a WGS reactor where carbon monoxide and water produce carbon dioxide and hydrogen (water-gas shift reaction). [5]

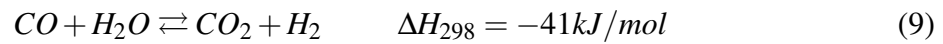
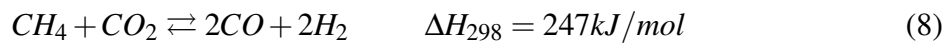
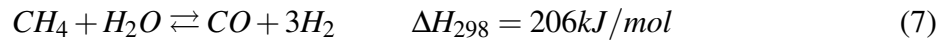
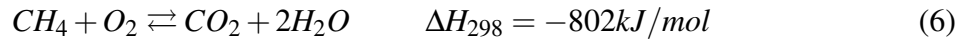


### 2.1.2 Partial oxidation (POX)

Another way to produce syngas is the partial oxidation of methane. This reaction needs 10-15% less energy than SRM, and the capitol cost is 25-30% cheaper compared to SRM. There are some problems that needs to be solved. For the reaction to go forward one needs co-feeding of oxygen under explosive conditions. The catalysts are exposed to carbon deposition, and from this there can be hot spots in the reactor. There are two reaction models that are accepted for this process. The first one is direct oxidation:



where methane and oxygen produce carbon monoxide and hydrogen. The other way for this is indirect oxidation that involves the methane combustion step that produce water and carbon dioxide. Then SRM and DRM reactions together with water-gas shift reaction are needed to produce syngas. [6]



### 2.1.3 Autothermal reforming (ATR)

ATR combines the two techniques of SRM and POX in a stand-alone process where the hydrocarbon conversion can be completed in one reactor, as shown in Figure 3.

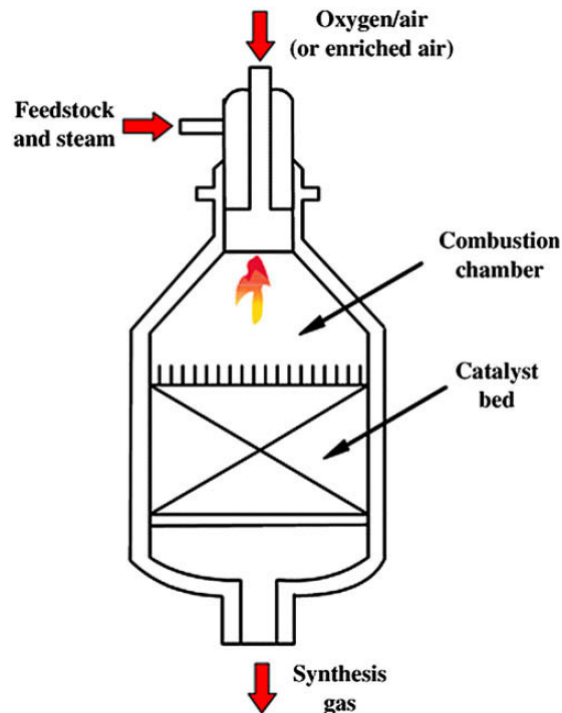
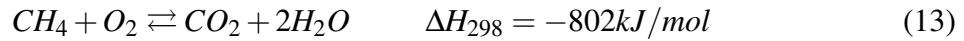
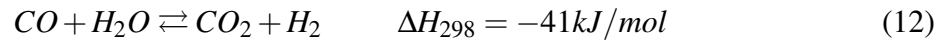
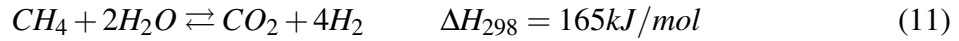
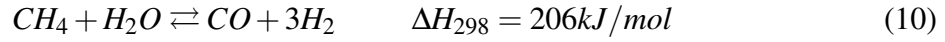


Figure 3: ATR reactor diagram [7]

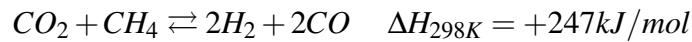
There are two types of ATR systems. The first one is used for fuel cell applications, consisting of a catalyst bed where combustion and steam reforming occur simultaneously. The second one has two separate sections. Non-catalytic partial oxidation occurs in the

first section using a burner. In the other section the steam reforming takes place on a catalyst bed. This type of reactor can be used for gas to liquid (GTL) applications. [7] The reactions used in the ATR process are a combination of SRM and POX. [8]



## 2.2 Dry reforming of methane (DRM)

Dry reforming of methane is that carbon dioxide (CO<sub>2</sub>) and methane (CH<sub>4</sub>) acts as reactants to form the products of hydrogen (H<sub>2</sub>) and carbon monoxide (CO), also known as syngas.



$$\Delta G^0 = 61770 - 67.32T(K)$$

This is an endothermic reaction that requires temperatures between 800 and 1000°C to give high equilibrium conversion to syngas, and to minimize carbon deposition on the catalyst during the reaction. The reason that the temperature is so high is that both methane and carbon dioxide are very stable molecules that requires a lot of energy (heat) to break up. [4] To try to decrease the necessary heat needed for the process, one can use different types of catalysts that will reduce the activation energy needed to transform reactants to products.

### 2.2.1 Side reactions

As the DRM proceeds, some side reactions are occurring simultaneously [1]

1. Reverse water-gas shift reaction:



$$\Delta G^0 = -8545 + 7.84T(K)$$

2. Boudouard reaction:



$$\Delta G^0 = -39810 + 40.87T \text{ (K)}$$

3. Methane decomposition:



$$\Delta G^0 = 21900 - 26.45T \text{ (K)}$$

At equilibrium, Gibbs free energy is equal to zero. For a reaction to proceed spontaneously to the right, producing products, Gibbs free energy must be less than zero. Because of this, RWGS and Boudouard reaction cannot occur at temperatures above 817°C and 701°C, respectively, while the methane decomposition reaction can only occur when the temperature is above 555°C.

DRM has a H<sub>2</sub>/CO ratio of about 1, but the Reverse Water-Gas Shift reaction (RWGS) can occur simultaneously with the DRM reaction, so the H<sub>2</sub>/CO ratio is therefore less than 1. The main challenge for the DRM reaction is carbon deposition on the catalyst. [1]

### 2.2.2 Kinetic models

There are 3 different kinetic models for the reaction rate of the DRM process: [9]

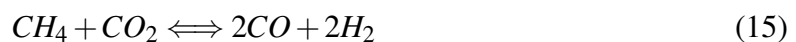
1. Power law model
2. Eley Rideal (ER)
3. Langmuir Hinshelwood-Hougen Watson (LHHW)

The power law is a simple model for reaction rate, expressed as

$$r = k[P_{CH_4}]^m [P_{CO_2}]^n \quad (14)$$

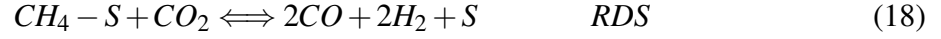
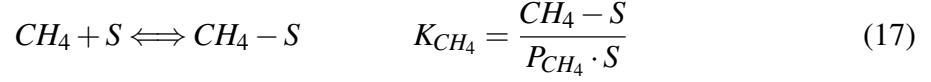
The simplicity of this model cannot explain the various mechanistic steps that are taking place on the surface of the catalyst. However, this model can be used as an initial estimate used to solve the more complicated models ER and LHHW.

The ER model is based on that one of the reactants is adsorbed on the catalyst surface at equilibrium. The adsorbed species that reacts with the other reactant from the gas phase lead to products. The basic reaction is



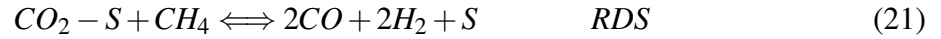
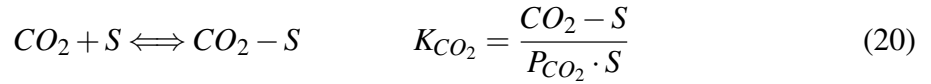
$$r_{Ref} = k_{Ref} \left( P_{CH_4} P_{CO_2} - \frac{P_{CO}^2 P_{H_2}^2}{K_{ref}} \right) \quad (16)$$

The first possible ER model is



$$r_{Ref} = \frac{k_{Ref} K_{CH_4} \left( P_{CH_4} P_{CO_2} - \frac{P_{CO}^2 P_{H_2}^2}{K_{ref}} \right)}{1 + K_{CH_4} P_{CH_4}} \quad (19)$$

The second possible ER model is



$$r_{Ref} = \frac{k_{Ref} K_{CO_2} \left( P_{CH_4} P_{CO_2} - \frac{P_{CO}^2 P_{H_2}^2}{K_{ref}} \right)}{1 + K_{CO_2} P_{CO_2}} \quad (22)$$

Both of the reactants can be the adsorbed species, resulting in two different models for ER. S is the active sites that are not being occupied in the mechanistic steps for all of the reactions, and RDS is the rate-determining step for the models.

Langmuir Hinshelwood-Hougen Watson (LHHW) is the most used model for the DRM reaction. In this model one assumes that there is one rate-determining step while the others are in thermodynamic equilibrium. [9] Table 1 gives an example of reactions that can be involved in the DRM reaction. [10] [11]

Table 1: Reactions in a DRM process

no.	Reaction	$\Delta H_{298}$ [kJ/mol]
1	$\text{CH}_4 + \text{CO}_2 \rightleftharpoons 2 \text{CO} + 2 \text{H}_2$	247
2	$\text{CO}_2 + \text{H}_2 \rightleftharpoons \text{CO} + \text{H}_2\text{O}$	41
3	$2 \text{CO} \rightleftharpoons \text{C} + \text{CO}_2$	-171
4	$\text{CH}_4 \rightleftharpoons \text{C} + 2 \text{H}_2$	75
5	$2 \text{CH}_4 + \text{CO}_2 \rightleftharpoons \text{C}_2\text{H}_6 + \text{CO} + \text{H}_2\text{O}$	106
6	$2 \text{CH}_4 + 2\text{CO}_2 \rightleftharpoons \text{C}_2\text{H}_4 + 2 \text{CO} + 2 \text{H}_2\text{O}$	284
7	$\text{C}_2\text{H}_6 \rightleftharpoons \text{C}_2\text{H}_4 + \text{H}_2$	136
8	$\text{CO} + 2 \text{H}_2 \rightleftharpoons \text{CH}_3\text{OH}$	-90.6
9	$\text{CO}_2 + 3 \text{H}_2 \rightleftharpoons \text{CH}_3\text{OH} + \text{H}_2\text{O}$	-49.1
10	$2 \text{CH}_3\text{OH} \rightleftharpoons \text{CH}_3\text{OCH}_3 + \text{H}_2\text{O}$	-37
11	$\text{CH}_3\text{OCH}_3 + \text{CO}_2 \rightleftharpoons 3 \text{CO} + 3 \text{H}_2$	258.4
12	$\text{CH}_3\text{OCH}_3 + \text{H}_2\text{O} \rightleftharpoons 2 \text{CO} + 4 \text{H}_2$	204.8
13	$\text{CH}_3\text{OCH}_3 + 3 \text{H}_2\text{O} \rightleftharpoons 2 \text{CO}_2 + 6 \text{H}_2$	136
14	$\text{CO}_2 + 4 \text{H}_2 \rightleftharpoons \text{CH}_4 + 2 \text{H}_2\text{O}$	-165
15	$\text{CO} + 3 \text{H}_2 \rightleftharpoons \text{CH}_4 + \text{H}_2\text{O}$	-206.2

At the temperatures that are normally used for DRM reaction (650-1000°C) the reactions that produce methanol and dimethyl ether (no. 5-7 in Table 1) does not occur. At high temperature it is more probable that the reactions 8 and 9 in Table 1 will proceed. This is because reactions 5-7 are exothermic, and 8 and 9 are endothermic. From this the reactions 8 and 9 are more favourable than reactions 5-7. Also, the reactions that produce ethane and ethylene are more prone to occur since these are also endothermic. Ethane and ethylene have appeared as side products in DRM reaction. Reactions that include  $\text{H}_2$  such as the reverse water-gas shift reaction (2), and the methanation reactions (14 and 15) could be observed at the high temperatures that are used in DRM reactions. [10] [11]

### 2.2.3 Deactivation of catalyst

The main problem for DRM reaction is the deactivation of the catalyst used in the process. There are two reactions that mainly lead to carbon deposition: methane decomposition and Boudouard reaction



When DRM reaction starts, the carbon deposition come from reaction (23) since there are only methane present in the system. When the time on stream (TOS) increases, CO

will also be present in the system. How much depends on the temperature and pressure for the reaction, where higher pressure favours the Boudouard reaction. Deactivation can occur from other ways, such as sulphur poisoning of catalyst or sintering of metal particles. There are some ways to prevent/control carbon deposition. One way is to increase the dispersion on the surface of the support. Supports that have high surface area ( $160\text{-}300\text{ m}^2/\text{g}_{\text{catalyst}}$ ) gives improved dispersion of active metals through their pore structure. Therefore, one gets a larger active surface area per unit weight of the active metal. Also increasing the basicity of the catalyst increases the resistance against deactivation for the catalyst. This occur because the rate of  $\text{CO}_2$  activation that oxidises surface carbon increases with increased basicity. [1]

### 2.3 Hydrotalcite derived catalysts

The gases  $\text{CH}_4$  and  $\text{CO}_2$  are very easy to obtain in nature and are therefore not very expensive. [12] Noble metals from group VIII are less sensitive to coke deposition than nickel (Ni), but are not thought for commercial use since they are very rare and expensive metals. [13] Nickel is cheaper and gives good activity for DRM, but are prone to deactivation due to coke deposition and sintering of the catalyst at high temperatures. Adding small amounts of the noble metals to nickel catalyst prevents against coking of the Ni catalyst. [14]

A new type of catalysts that has gained increased attention over the recent years, are catalysts where hydrotalcite (HT) is used as a precursor. The catalysts have then shown better resistance against carbon formation and thermal sintering. Adding rhodium (Rh) to the catalysts improve the resistance against carbon formation on the catalysts. [1]

The name HT originates from a naturally occurring layered mineral discovered in Sweden in 1814. The mineral has a chemical structure that resembles talc, with a high content of water. The structure consists of octahedrons with a divalent or trivalent metal in the center, and 6 hydroxyl molecules around it. The layered sheets of the HT are then built up by interchanging divalent and trivalent metals which makes the layers positively charged. To neutralize the charge there are anions and water molecules in the interlayer structure of the HT. Figure 4 displays a simple illustration of the structure of HTs.



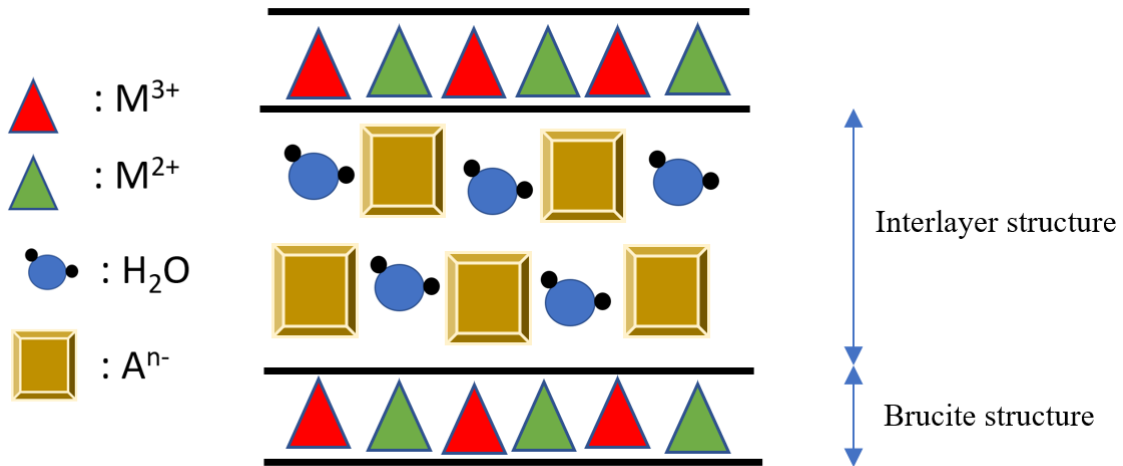


Figure 4: The general build-up structure of hydrotalcites

Today the name hydrotalcite or layered double hydroxides (LDH) is describing a large number of synthesized minerals that have a similar structure to the mineral discovered in Sweden. These have the general formula

$$[M_{1-x}^{2+}M_x^{3+}(OH)_2]^{x+}[A_{x/n}^{n-}]^{x-} \cdot mH_2O \quad (25)$$

where  $M^{2+}$  consists of two metals with a valence of  $2^+$  and  $M^{3+}$  consists of one metal with valence of  $3^+$ .  $A^-$  is a negative charged ion that balances the charge in the interlayer structure. [9]  $n$  is the charge of the anion, and is in the range between 1-6.  $m$  is the number of water molecules in the interlayer structure, and is zero or a positive number.  $x$  is the mole fraction of the  $M^{3+}$  metal [15] [16] [17], calculated as

$$x = \frac{M^{3+}}{M^{2+} + M^{3+}} \quad (26)$$

where  $M^{2+}$  and  $M^{3+}$  are the total moles of the divalent and trivalent cations, respectively. To create stable layers for the HT structure, the size in radii of the ions for the divalent and trivalent metals should not be very different from the size of  $Mg^{2+}$  (0.072 nm) and  $Al^{3+}$  (0.054 nm) ions. To form a pure LDH phase,  $x$  should be between 0.2-0.4. If the value are outside this range, other types of hydroxides or compounds can be formed. To obtain the purest structure for hydrotalcites,  $x$  should be 0.25. [17] [18] [19]

To transform a HT to a mixed oxide, the catalyst can be heated at a certain temperature (calcination process), where the catalysts go through four steps: 1). dehydration, 2). dehydroxilation, 3). decomposition of anion, 4). oxide reformation. In step 4). the mixed oxides are formed when the temperature is above  $450^\circ C$ . [18]

Another ability of hydrotalcites is the "memory-effect", where the initial hydrotalcite structure can be reconstructed after hydration of the catalyst. By adding a noble metal solution to the calcined HT, a new layer can be developed, and noble metals can replace one of the divalent/trivalent cations, or they can be trapped in one of the layers of the HT. This will improve the abilities of the catalyst such as better activation and increased stability against sintering. The forming of this new layer can be done if the calcination temperature has been  $< 600^{\circ}\text{C}$ , and if the calcined catalyst is exposed to water. [18] [20] [21]

HT can easily be synthesized from the co-precipitation method. Often the HTs are used as precursors for catalysts, since when calcined the HTs can form mixed metal oxides that improves important properties of a catalyst. Among the properties there are high surface area, small particle size, increased basicity and improved thermal stability against deactivation. The divalent and trivalent cations are evenly distributed in the layers, leading to a homogeneous mixture of oxides. [9] [22] [23] [24] [25]

## **2.4 Theoretical background for the experiments**

### **2.4.1 Co-precipitation and Incipient Wetness impregnation**

For Co-precipitation a solution of salts of both the active material and the support component are prepared. A precipitating agent, such as NaOH and/or  $\text{Na}_2\text{O}_3$  is mixed together with the solution to prepare the catalyst. This changes the pH of the solution, which lead to formation of oxides or hydroxides. Additional ions can be introduced into the solution to exceed the solubility of one of the precipitating elements. The final catalyst is then filtrated and washed to get the solid material wanted before drying. [26] [27]

Impregnation is that a support-metal is mixed with a liquid solution, normally water solution, and then the precursor is dropped slowly onto the support. The different types of impregnation is explained by the relationship between the impregnated liquid volume,  $V_{imp}$ , and the pore volume of the support material,  $V_P$ . The difference between the methods is whether  $V_{imp} \approx V_P$ , or if  $V_{imp} > V_P$ . Incipient wetness (IW) belongs to the category that  $V_{imp} \approx V_P$ , and liquid solution is used to impregnate the support material. Capillary pressure is the driving force that fills the pores. The method can be done quickly because the support material takes up the liquid very fast. [26]

### **2.4.2 Calcination**

The calcination procedure exposes the catalyst to a high temperature to finalize the formation of a metal oxide catalyst in a gaseous atmosphere inside either a furnace or reactor. Calcination is done primarily to remove all impurities of the catalyst, leaving the surface area free of any impurities that can poison the final catalyst. The temperature is slowly increased at a ramp rate, normally in degrees/min. When the desired temperature for the

process is reached, the process will then hold at this temperature for the time that is set, and then the system is turned off. The gas flow rate during calcination, and the cooling rate when the system is turned off are considered to be negligible for the outcome of the process. The optimal calcination temperature for Ni-Mg-Al HT precursors prepared from co-precipitation method is 600°C. [17] [26]

### 2.4.3 Specific surface area, pore volume and pore size distribution

The pores of a heterogeneous catalyst are characterized after their size into four different categories:

1. ultramicroporous:  $< 0.7$  nm
2. microporous:  $< 2$  nm
3. mesoporous: 2-50 nm
4. macroporous:  $> 50$  nm

The category for the most common measuring methods mentioned in the following sections is in the mesoporous size range. The shape of the pores are normally irregular. The closest form of geometric shape are cylindrical, slits and voids. Cylindrical and slits are the geometrical models most used since they are simpler to handle mathematically. Alumina ( $\text{Al}_2\text{O}_3$ ) and Magnesia ( $\text{MgO}$ ) are examples of oxides that have cylindrical pores. [28]

#### 2.4.3.1 $\text{N}_2$ adsorption/desorption procedure

The standard procedure for measuring specific surface area, pore volume and pore size distribution is  $\text{N}_2$  adsorption/desorption at 77 K. The first step is the determination of adsorbed volume of nitrogen against relative pressure. IUPAC (International Union of Pure and Applied Chemistry) have classified 6 types of adsorption isotherms where the four presented in Figure 5 are the ones usually found for catalysts.

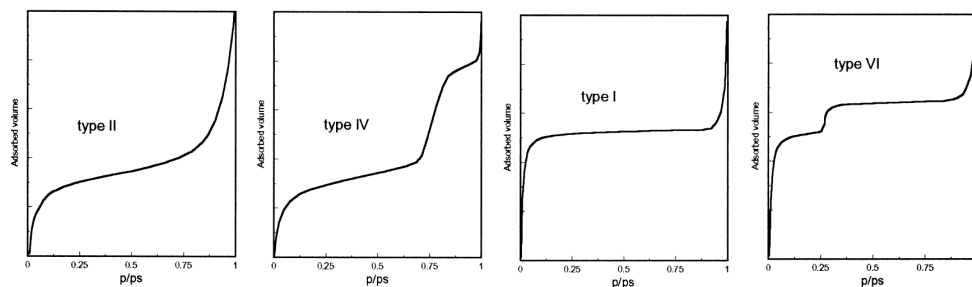


Figure 5: Adsorption isotherms from  $\text{N}_2$  adsorption [28]

Most catalysts belong to the class IV isotherm that represents mesoporous solids. Type II isotherm represents macroporous solids. The isotherm is presented as a figure with adsorbed volume of N<sub>2</sub> versus relative pressure ( $\frac{P}{P_0}$ ). When saturation is reached, evaporation from the pores begin. This proceeds at a lower relative pressure, and therefore give a hysteresis curve as a result for the complete adsorption/desorption process. This is because different catalysts can have different pore shape. The six main types of hysteresis have been identified after the IUPAC classification as shown in Figure 6

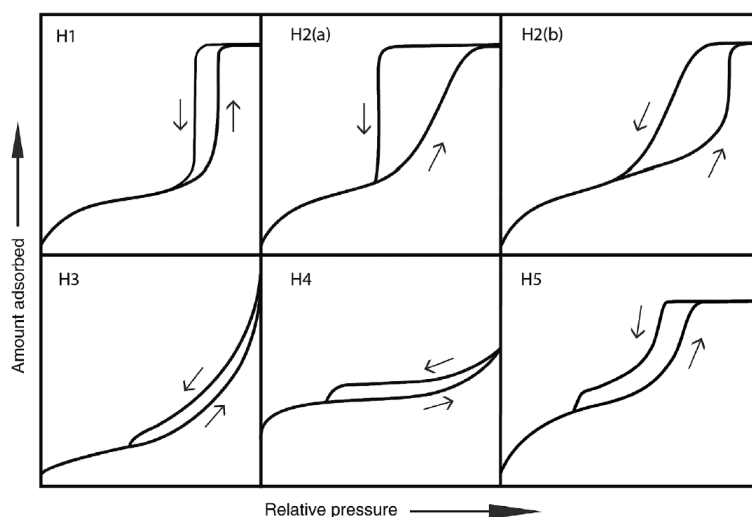


Figure 6: The six hysteresis shapes from the N<sub>2</sub> adsorption/desorption isotherm [29]

The hysteresis type of H1, H2(a) and H2(b) are the ones that are common for catalysts and carriers. Type H1 hysteresis have either cylindrical channels, or are made up by agglomerates of spherical particles which lead to a narrow distribution of uniform mesopores. The steep and narrow form of the curve suggests that there is a delayed condensation on the adsorption part. Templated silicas and mesoporous carbons usually gives this type of hysteresis form. Type H2 hysteresis loops are representing more complex pore structures. The steep desorption part can be described as pore blocking in a narrow range of pore necks, or it could be to evaporation induced by cavitation. Silica gels and some ordered mesoporous materials show these kind of hysteresis forms. Pore blocking is also a part of H2(b) hysteresis, but here the size distribution for the width of the pore necks are much larger. The hysteresis curves for H3 and H4 are common for active carbons and zeolites. The solids representing these types of hysteresis curves are consisting of aggregates with plate like particles that form slit shaped pores. The difference is that H3 type have a type II adsorption isotherm, while H4 is composed of both type I and type II adsorption isotherm. The H5 hysteresis curve is not so common. This type describes pore structures that contains both open and partially blocked mesopores. The H3, H4 and H5 curves have a steep form for the desorption part of the curve that makes them easy to recognize. This is generally located at narrow ranges for a relative pressure ( $P/P_0$ ) between 0.4 and 0.5 for nitrogen. [28] [30]

### 2.4.3.2 BET surface area

To measure the specific surface area,  $S$ , of a sample, the BET method after Brunauer, Emmett and Teller (1938) is the standard method used for this. The procedure is that gas is being physically adsorbed on the surface of the sample, and then the volume of adsorbed gas corresponding to a monolayer surface of the sample is being calculated. Nitrogen ( $N_2$ ) is the common gas used for this at its boiling temperature of  $-196^\circ\text{C}$  (77 K). [31] The BET equation for determining the monolayer volume is

$$\frac{V}{V_m} = \frac{C\left(\frac{P}{P_0}\right)}{\left[1 + (C - 1)\frac{P}{P_0}\right] \cdot \left[1 - \frac{P}{P_0}\right]} \quad (27)$$

where  $V_m$  is the monolayer volume at standard conditions (S.C.) that is used to calculate  $S$ .  $V$  is the adsorbed volume (at S.C.), and  $\frac{P}{P_0}$  is the partial vapour pressure of the adsorbate gas divided on the saturated pressure of the adsorbate gas.  $C$  is the BET constant, which is given by the formula

$$C = \frac{e^{q_1 - q_L}}{RT} \quad (28)$$

where  $q_1$  is the heat adsorption for the first layer on the surface, and  $q_L$  is the heat from condensation that is equal for all the layers except the first one. To estimate a value for  $C$  and  $V_m$ , equation (27) can be re-written into a linear form of  $y = a + bx$ , where  $a$  is the intercepting point and  $b$  is the slope.

$$\frac{\frac{P}{P_0}}{V\left(1 - \frac{P}{P_0}\right)} = \frac{1}{CV_m} + \frac{(C - 1)}{CV_m} \cdot \frac{P}{P_0} \quad (29)$$

where  $a = \frac{1}{CV_m}$  and  $b = \frac{C-1}{CV_m}$ . When plotted with a low pressure value in the range of  $0.05 < \frac{P}{P_0} < 0.25$ , the result should give straight lines in the plot. [32] From this the BET constant,  $C$ , can be calculated as  $\frac{b}{a} + 1$ , and the monolayer volume,  $V_m$ , as  $\frac{1}{b+a}$ . The specific surface area,  $S$ , can then be calculated from the formula

$$S = \frac{V_m NA}{22414 \times m} \quad (30)$$

where  $N$  is Avogadro's number,  $A$  is the cross-sectional surface area where one single gas molecule has been adsorbed,  $m$  is the mass used in the experiment, and the number 22414 is the volume of one mole of gas at standard conditions. [31] [33]

### 2.4.3.3 BJH pore volume and size

To measure the pore volume and pore size distribution, the method after Barrer, Joinyer and Halenda (BJH-method) is the standard one used today. It is based on the Kelvin equation and modified for mesopore measurement

$$\ln\left(\frac{P}{P_0}\right) = -\frac{2\gamma V_m \cos(\theta)}{RT r_c} \quad (31)$$

where  $r_c$  is cylindrical pore radius,  $\gamma$  is surface tension,  $V_m$  is molar volume and  $\theta$  is the contact angle between the adsorbed layer and the pore wall.  $R$  is the universal gas constant, and  $T$  is temperature.

A pressure increase in the capillary condensation area, when  $\frac{P}{P_0} > 0.4$ , causes an increase in the thickness of adsorbed layer on the pore walls. It also increases the capillary condensation in the pores that have a core size  $r_c$ . By assuming that the pores have a geometrical shape, in our case cylindrical, the core volume and core size can be transformed into pore volume and pore size. The pore volume and pore size distribution can then be obtained by examining the isotherm step by step from  $0.42 < \frac{P}{P_0} < 0.98$ . [28] [34]

### 2.4.4 Crystallography and X-ray Diffraction (XRD)

X-rays is electromagnetic radiation with a relatively short wavelength,  $\lambda$ . To examine crystallographic directions and distances between the atoms in a crystal, one can look at the crystal as an unit cell. The unit cell is visualized by imaginary planes with various orientations, and each of the orientations is intercepting translation vectors at various points. The characterization of each cell is then represented by a integer, given by the inverse of the point of where the axial part of the planes intercept with each other. The description of the direction and distance is given as Miller indices. Parallel planes will meet at infinity and they are given the Miller indice of zero, since the inverse of infinity goes to zero mathematically. The Miller indices define the length of the imaginary planes from the edges of the unit cell. From this the unit cell and thus the crystal structure is presented as the perpendicular distance between the planes as a distance vector,  $\mathbf{d}_{h,k,l}$ , which gives the distance between the atoms.  $h, k$  and  $l$  define the different axes of the plane. As an example, a plane that passes through each unit cell is intercepting the  $\mathbf{h}$  axis at  $1/1$ , the  $\mathbf{k}$  axis at  $1/2$ , and is Parallel to the  $\mathbf{l}$  axis has Miller indices of  $1/1, 1/2$  and  $1/\infty$ , or  $(120)$ . If the plane passes in the negative sign of an axis, the number gets a bar over it, e.g.  $(1\bar{2}0)$ . [35]

#### 2.4.4.1 Diffraction and Bragg's law

When waves that are scattered from an object interfere constructively and destructively

with each other, we have diffraction. These waves are characterized by their wavelengths,  $\lambda$ . A wave will scatter from an object in all directions. A second wave is scattered from another object at a given wavelength distance from the first scattered wave. The two scattered waves can then be viewed to be in phase at some angle. W.L. Bragg was the first to prove that the phenomena of diffraction can be described mathematically as a general law.

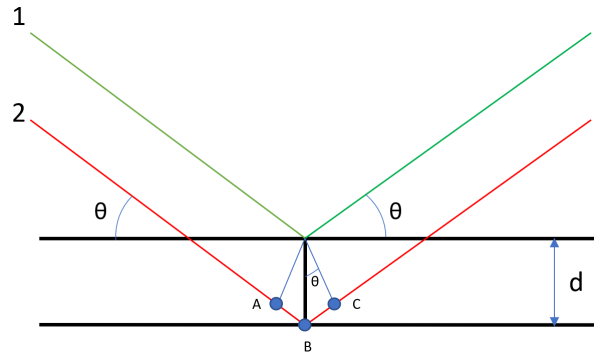


Figure 7: Diffraction of two X-ray beams

This is explained as the atoms in a unit cell is exposed to two X-ray beams, there will be diffraction in all directions for each of the beams. As shown in Figure 7, the second beam must travel a distance  $AB + BC$  further than the first beam to be in phase. This will only happen if the distance  $AB + BC$  is an integer of the wavelength  $\lambda$ , which gives the equation  $n\lambda = AB + BC$ . From Figure 7 one can see from trigonometry that  $AB + BC = 2 AB$ , and  $\sin \theta = \frac{AB}{d}$ . So  $AB = d \sin \theta$  and  $n\lambda = 2 AB$  gives Bragg's law [35]

$$n\lambda = 2d \sin(\theta) \quad (32)$$

#### 2.4.4.2 X-ray Powder Diffraction and Scherrer equation

Every atom is unique in the way that its size and scattering ability is not equal to any other atom. Because of this the distance between the planes  $d_{h,k,l}$ , and the intensities of the X-ray beams are unique for each material. A material is built up of many different atoms, and the diffraction angle is therefore different for each of the materials that are being measured by X-ray diffraction. As already seen, a single crystal will give an angle  $\theta$  when exposed to a X-ray beam which is determined by the distance between the planes. Since the material that are being measured is in a powder form, it will consist of much more than just a single crystal, but millions to billions of smaller crystallites. When measured in a X-ray beam, the powder will represent all the planes, but diffraction will only happen at the diffraction angle for each plane. If the angle the X-ray detector is using is changed from  $\theta$  to  $2\theta$ , it will detect all possible diffraction peaks that is produced from the crystallites in the powder measured. [35] To get an approximate value for the particle

size of crystallites, the Scherrer equation can be used

$$d_{avg.} = \frac{k\lambda}{\beta \cos(\theta_0)} \quad (33)$$

where  $\lambda$  is the wavelength,  $\theta_0$  is the angle given for the maximum diffraction peak and  $\beta$  is the breadth given at full width of half maximum intensity (FWHM).  $k$  is a constant also known as the shape factor, which is equal to 0.9 when  $\beta$  for FWHM is used. [36]

To identify the different materials a powder diffraction database exists to determine different diffraction patterns. The International Centre for Diffraction Data (ICDD) is a non-profitable organization that publishes the *Powder Diffraction File* which contains about 60000 different patterns. [35]

#### 2.4.5 Chemisorption

Chemical adsorption (chemisorption) is an important analytical tool for evaluation of catalysts. Chemisorption takes place when gas molecules are being adsorbed and bound onto a solid surface. The gas molecules are called the *adsorptive* when it is not bound to anything, and *adsorbate* while it is bound to the solid surface. The solid surface is called *the adsorbent*. Chemisorption is that a chemical bond consisting of electrons shared between the adsorbate and the adsorbent forms on a surface. The powerful strength of the chemical bond makes chemisorption very difficult to reverse. Chemisorption can only occur between certain adsorptive and adsorbent species, and only if the surface is cleaned of previously adsorbed molecules. As long as the adsorptive can make contact with the surface, chemisorption can proceed. The adsorption isotherm is the relationship between quantity of molecules adsorbed and the pressure at a constant temperature. The chemisorption isotherm evaluates the surface only at areas that are capable of forming a chemical bond with the gas molecules. Important characteristics measurable are metal dispersion of the catalyst and the crystallite size.

The percentage of metal dispersion is the available quantity of active molecules divided by the total number of active molecules times 100%.

$$M\% = \frac{N_s}{N_T} \cdot 100\% \quad (34)$$

where  $N_s$  is the number of surface atoms calculated from

$$N_s = F_s \cdot N_m \quad (35)$$

$F_s$  is the stoichiometry factor and  $N_m$  is the number of adsorptive molecules.



The crystallite size of the particles are calculated based on the geometrical shape of the catalyst, usually a sphere. From this chosen geometry the diameter of a grain molecule can be determined by area and volume. The actual volume of the active metal is unknown, but molecular density is known. The volume can then be expressed as area times density. The average diameter of the active metal grains can then be calculated by [37]

$$D = \frac{6}{\rho_m A_m} \quad (36)$$

where  $D$  is the average diameter [m],  $\rho_m$  is the molecular density [ $\text{g}/\text{m}^3$ ], and  $A_m$  is the area per unit mass of the metal [ $\text{m}^2/\text{g}$ ].

#### 2.4.6 Temperature Programmed Reduction/Desorption (TPR/TPD)

To get information on the temperature needed for complete reduction of a catalyst, TPR is commonly used today. A standard set up for TPR is shown in Figure 8. A typical experiment for TPR is that a finite mass of the catalyst powder, 0.1-2.0 g, is placed on quartz wool in a quartz tube. The tube is then locked in a furnace. The sample could be pre-treated in  $\text{O}_2$  gas to have a reference state of it before the experiment begins. Then the oxygen is replaced with the  $\text{H}_2/\text{Ar}$  gas. The linear temperature begins when the detector system has stabilized. A processor is controlling the temperature, normally with a heating rate between  $0.1$  and  $20^\circ \text{C}/\text{min}$ . The gas is measured by a thermal conductivity detector (TCD). To optimize the thermal conductivity difference between the reactant gas and the carrier gas, a mixture of 5%  $\text{H}_2$  in Argon (Ar) is used. Controllers are in place to ensure stable flow of the gases. The gas flows through the sample and further through a cold trap that condenses the produced water before it is measured in the TCD. For pre-treating and purging purposes, additional gas lines are also installed in the system. A computer is measuring and recording the  $\text{H}_2$  consumption simultaneously as the temperature is measured by the thermocouple connected with the sample. [36] [38]

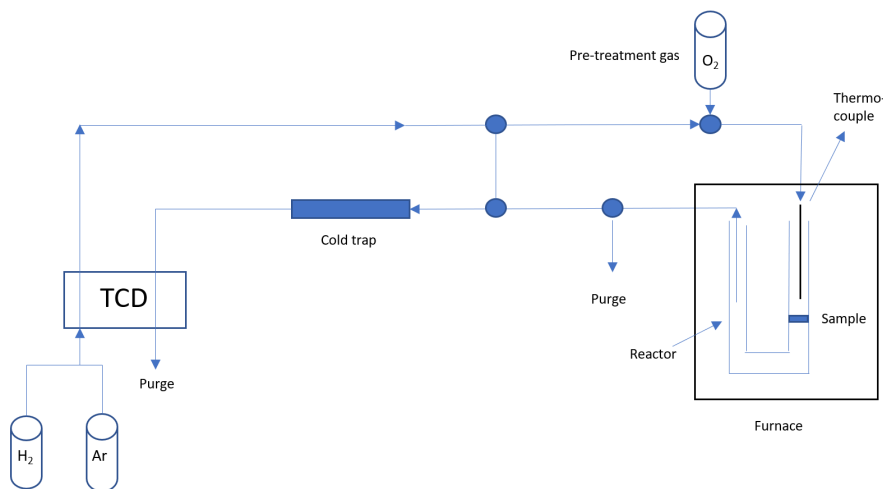


Figure 8: Simplified schematic representation of the TPR/TPD instrument [36]

The result of TPR is presented as a figure with temperature on the x-axis, and the detection signal for H<sub>2</sub> consumption on the y-axis. [39] The area under the curve in the graph is the total hydrogen consumption, expressed as moles of H<sub>2</sub> consumed per mole of metal atoms. TPR is a good method to get the reducibility of a metallic catalyst. [38]

Results from the TPR experiment are said to be representative if the assumption that the mean hydrogen concentration between inlet and outlet is what drives the reaction forward is fulfilled. To achieve this, two criteria have to be checked: 1). for the point where we have maximum hydrogen consumption, the amount of hydrogen consumed at this point should not exceed 2/3 of the amount of hydrogen gas fed into the reactor, and 2). there should be a minimum conversion of 10% at the maximum peak for hydrogen consumption. From these criteria a sensitivity factor,  $K$  [s], has been defined to get range of when we can get representative results. [39]

$$K = \frac{S^\circ}{V \cdot C^\circ} \quad (37)$$

where  $S^\circ$  [ $\mu\text{mol}$ ] is the initial amount of reducible species in the sample.  $V$  is the total flow rate [ $\text{cm}^3/\text{s}$ ] and  $C^\circ$  is the hydrogen concentration in the carrier gas [ $\mu\text{mol}/\text{cm}^3$ ]. The range of  $K$  has to be between 55-140 s. For values below 55 s, the sensitivity of the experiment becomes too low. If the values are above 140 s the amount of reducing gas is too high, which will violate the assumption that there is a linear concentration profile. When  $K$  is optimized, a resolution parameter,  $P$ , can be determined when the influence of the heat rate,  $\beta$ , is taken into account. To ensure a good resolution for the experiment,  $P$  must be less than 20. [19] [39] [40] [41]

$$P = \beta \cdot K \quad (38)$$

Temperature programmed desorption are used to determine the basicity at the surface of the different catalysts, which measures the rate of desorption of adsorbed CO<sub>2</sub> molecules as a function of temperature. The procedure is to increase the temperature for the sample while the desorption of the adsorbate is monitored. As for the TPR, the sample is placed in a quartz tube inside a furnace, as shown in Figure 8. For TPD the standard method is to increase the temperature with a constant heating rate between 0.5°C/s and 25°C/s. A TPD profile can be used to get two different types of data. The area under the graph can be used to determine the surface coverage. The graph gives peaks where the activation energy for desorption are highest. The higher temperature for the peaks, the more difficult it is for desorption to occur. This is an indication of the strength of interaction between the active sites on the surface of the catalyst and the adsorbates. [39]

### 3 Experimental work

#### 3.1 Catalyst preparation

The general equation for HTs is given from equation (39)

$$[M_{1-x}^{2+}M_x^{3+}(OH)_2]^{x+}[A_{x/n}^{n-}]^{x-} \quad (39)$$

where x is the mole fraction of  $Al^{3+}$ .

The  $Ni^{2+}$  -  $Y^{2+}$  -  $Al^{3+}$  HT catalysts was prepared after the method of Bhattacharyya et al (2000) [16], with some small modifications.  $Y^{2+}$  represents the divalent metals used;  $Mg^{2+}$  and  $Ca^{2+}$ . In all catalysts, the  $Al^{3+}$  was maintained at a molar percentage  $x = 0.25$ , which gives a  $\frac{Ni^{2+}+Y^{2+}}{Al^{3+}}$  molar ratio of 3:1. Two more catalysts were made by adding different amounts of Rhodium (Rh) to the 20NiMgAl catalyst. The procedures for the calculation of the total mass for the different catalysts are shown in Appendix A. The denotation and metal content (wt %) of the different catalysts are displayed in Table 2

Table 2: Denotation and metal content (wt %) of the catalysts

Denotation	Ni	Mg	Ca	Al	Rh
12NiCaAl	12		63	25	
20NiCaAl	12		55	25	
12NiMgAl	12	63		25	
20NiMgAl	20	55		25	
20NiMgAlRh(0.1)	20	55		25	0.1
20NiMgAlRh(0.5)	20	55		25	0.5

All chemicals were purchased from Merck Millipore unless otherwise stated. The chemicals were used without any further treatment. The chemicals used are nickel(II) nitrate hexahydrate ( $Ni(NO_3)_2 \cdot 6H_2O$ ), magnesium nitrate hexahydrate ( $Mg(NO_3)_2 \cdot 6H_2O$ ), calcium nitrate tetrahydrate ( $Ca(NO_3)_2 \cdot 4H_2O$ ) [Alfa Aesar], aluminum nitrate nonahydrate ( $Al(NO_3)_3 \cdot 9H_2O$ ), rhodium(III) nitrate hydrate ( $Rh(III)(NO_3)_3 \cdot xH_2O$ ) [Sigma Aldrich], sodium hydroxide (NaOH) [VMR], sodium carbonate ( $Na_2CO_3$ ) and nitric acid ( $HNO_3$ ) [VMR].

$Ni(NO_3)_2 \cdot 6H_2O$ ,  $Mg(NO_3)_2 \cdot 6H_2O$  or  $Ca(NO_3)_2 \cdot 4H_2O$  and  $Al(NO_3)_3 \cdot 9H_2O$  was used as metal precursors (cations).  $Na_2CO_3$  and NaOH acted as precipitants (anions).

For each prepared catalyst stoichiometric amounts of  $Na_2CO_3$  and NaOH were dissolved in 400 ml deionized water. The other solution with calculated stoichiometric amounts of  $Ni(NO_3)_2 \cdot 6H_2O$ ,  $Mg(NO_3)_2 \cdot 6H_2O$  or  $Ca(NO_3)_2 \cdot 4H_2O$ , and  $Al(NO_3)_3 \cdot 9H_2O$  were dissolved in 400 ml deionized water. The precursor solution was added dropwise to the

basic solution under continuous stirring at room temperature. When the addition was completed, the gel-like mixture was adjusted to a pH between 9-10 with nitric acid, and aged at 85° C under continuous N<sub>2</sub> purge and stirring for 18 hours, as presented in Figure 9.

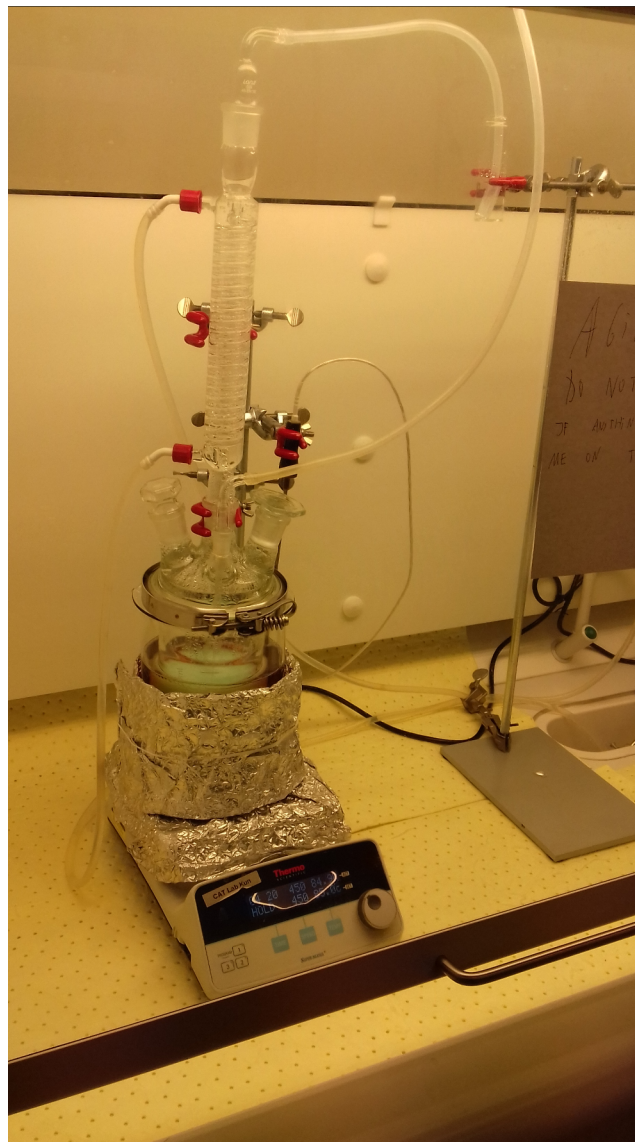


Figure 9: Set-up of the aging process.

The cooled sample was suction-filtered, and washed with deionized water until the pH was measured to be 7 by a pH-paper. Then it was dried at 90°C for 24 h.

The 12NiMgAl and 20NiMgAl catalysts were calcinated in flowing air at 600°C for 6 h, where the temperature was raised at a ramp up rate of 5°C/min. The 12NiCaAl and 20NiCaAl catalysts were calcined without air in a Nabertherm P330 furnace at 800°C for 6 h, with an increasing rate of 5°C/min. The setup for calcination is presented in Figure 10.



Figure 10: Set-up of the calcination process

Rhodium was added from  $\text{Rh(III)(NO}_3)_3 \cdot x\text{H}_2\text{O}$  to the 20NiMgAl catalyst by the incipient wetness method (IW). About 2 ml of DI water was used in the process to dissolve the rhodium salt. These samples were dried at  $80^\circ\text{C}$  overnight and calcined at  $600^\circ\text{C}$  for 6 h with an increasing temperature rate of  $5^\circ\text{C}/\text{min}$ . A summary of the processes is presented in Table 3.

Table 3: Summary of catalyst preparation processes

Catalyst	pH	Aging	Drying	Calcination
12NiCaAl	9.84	$85^\circ\text{C}$ for 18 h	$90^\circ\text{C}$ for 24 h	$800^\circ\text{C}$ for 6 h
20NiCaAl	9.75	$85^\circ\text{C}$ for 18 h	$90^\circ\text{C}$ for 24 h	$800^\circ\text{C}$ for 6 h
12NiMgAl	10.00	$85^\circ\text{C}$ for 18 h	$90^\circ\text{C}$ for 24 h	$600^\circ\text{C}$ for 6 h
20NiMgAl	9.00	$85^\circ\text{C}$ for 18 h	$90^\circ\text{C}$ for 24 h	$600^\circ\text{C}$ for 6 h
20NiMgAlRh(0.1)	-	-	$80^\circ\text{C}$ overnight	$600^\circ\text{C}$ for 6 h
20NiMgAlRh(0.5)	-	-	$80^\circ\text{C}$ overnight	$600^\circ\text{C}$ for 6 h

## 3.2 Catalyst characterization

N<sub>2</sub> adsorption/desorption measurements were done in a Micromeritics TriStar II apparatus with N<sub>2</sub> at 77 K. The samples were degassed in a Micromeritics VacPrep 061 Sample Degas System at 180°C overnight to remove impurities. Specific surface area (SSA) was calculated by using the BET method, while pore volume and pore size distribution was calculated by the BJH method.

XRD measurements were performed in a Bruker-AXS (D8 Advanced) Microdiffractometer with Cu K $\alpha$  as the radiation source. The instrument has  $\lambda = 1.5418$  [Å], voltage = 40 [kV] and current = 25 [mA]. The scanning procedure was set to  $2\theta$  in the range of 5-90°, with a ratio of 1°/min. The resulting peaks were compared with the Joint Committee on Powder Diffraction Standards (JCPDS) database.

Temperature programmed reduction (TPR) and carbon dioxide temperature programmed desorption (CO<sub>2</sub>-TPD) were performed in a Micromeritics Autochem II ASAP 2090 apparatus with a thermal conductivity detector (TCD) to measure the H<sub>2</sub> consumption and CO<sub>2</sub> adsorption. 0.1225 g of catalyst was used in the experiment to get the right result in comparison to sensitivity and resolution factor. The calculations for this are shown in Appendix B. The catalyst was inserted on top of quartz wool in a U-tube, and then locked inside a furnace as it is shown in Figure 8.

Before the TPR experiment the catalyst was pretreated in helium (He) flow at 200°C, then it was cooled down to 50°C. The experiment was then performed with a gas mixture consisting of 10% hydrogen (H<sub>2</sub>) in Argon (Ar) at a flow rate of 50 ml/min. The temperature was increased with a ramp rate of 10 °C/min from 50 to 950°C. The CO<sub>2</sub>-TPD experiment was done when TPR was finished, so the same amount of sample was used for this experiment as well. For TPD the sample was pretreated at 600 °C with helium, with a temperature rate of 10°C/min, before cooled down to 80°C with a cooling rate of 10°C/min also under helium flow. Then the sample was held at 80°C in a gas flow consisting of 6% CO<sub>2</sub> in Ar for 1 h, before TPD was performed from 50-800°C with a heating rate of 10°C/min in a He flow.

To measure the metallic surface area and metal dispersion of the catalysts, H<sub>2</sub>-chemisorption was performed in a Micromeritics ASAP 2020 Plus apparatus. For chemisorption the sample was first reduced with flowing H<sub>2</sub> at 600°C for 4 hrs, with an increasing rate of 5°C/min. The sample was then cooled in N<sub>2</sub> flow down to 35°C, with a cooling rate of 10°C/min and held at this temperature for 1 h. The measurements were then performed at 35°C with 20 measurement points in the range of 1 to 550 mmHg.

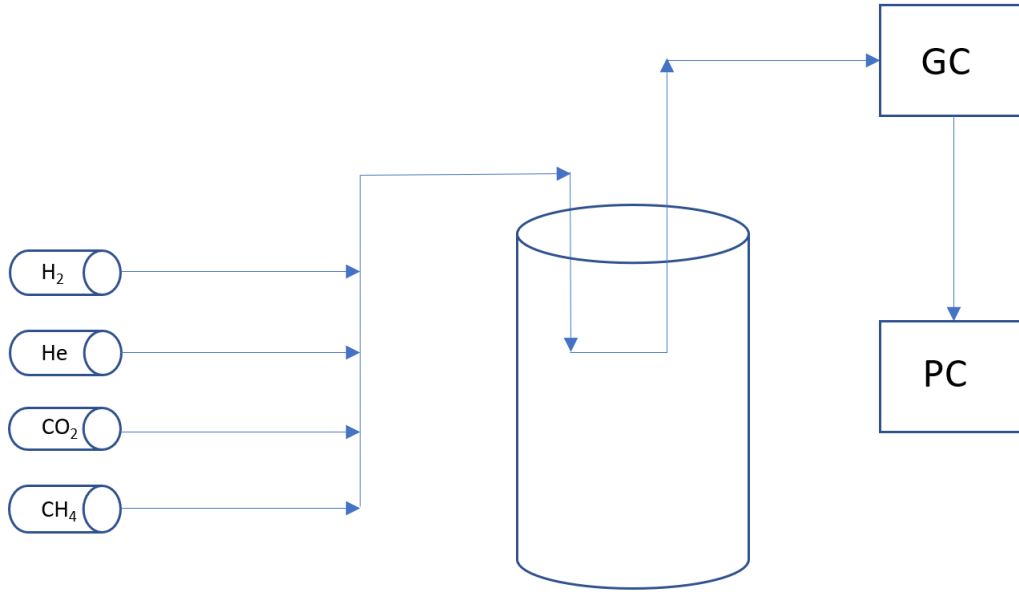


Figure 11: DRM reaction schematic

The setup for the DRM reaction is shown in Figure 11 where the catalytic testing was performed in a cylindrical fixed-bed reactor with an inner diameter of 11.81 mm at 1 bar. A catalyst bed consisting of 50 mg of catalyst mixed with 500 mg of  $\alpha$ -Al<sub>2</sub>O<sub>3</sub> was placed on top of a quartz wool plug, which was held in place with a catalyst tube supporter. To control the temperature during the test, a type K Eurotherm thermocouple was installed on the top of the catalyst bed. [42] The catalyst was first reduced in a 100 ml/min flow of H<sub>2</sub>/N<sub>2</sub> with 50/50 ratio at 600°C. The temperature ramp up rate was 5°C/min. When the temperature reached 600°C, the gas flow was switched to 100 ml/min of N<sub>2</sub>. The temperature continued to increase at 5°C/min in N<sub>2</sub> flow until it reached the reaction temperature of 750°C. This flow and temperature was then held for 30 min, before the gas flow was changed to 200 ml/min with a 50/50 percentage mix of CO<sub>2</sub> and CH<sub>4</sub>, giving a gas hourly space velocity (GHSV) of  $240000 \frac{ml}{g_{cat} \cdot hr}$ . The reaction was run for 15 hrs. To measure the reactants and products after the reaction, an Agilent 7890B Gas Chromatograph (GC) System with two TCDs was used. The conversion of the products and the ratio between H<sub>2</sub>/CO was calculated from the following equations

$$X_{CH_4} = \frac{(F_{CH_4})^{in} - (F_{CH_4})^{out}}{(F_{CH_4})^{in}} \cdot 100\% \quad (40)$$

$$X_{CO_2} = \frac{(F_{CO_2})^{in} - (F_{CO_2})^{out}}{(F_{CO_2})^{in}} \cdot 100\% \quad (41)$$

$$\frac{H_2}{CO} = \frac{(F_{H_2})^{out}}{(F_{CO})^{out}} \cdot 100\% \quad (42)$$

where F represents the flow in ml/min at inlet and outlet of the reactor. [14]

## 4 Results and discussion

### 4.1 X-ray diffraction

Figure 12 presents the XRD diffraction pattern for the as-prepared precursors before calcination. To illustrate the peaks of the NiMgAlRh catalysts more clearly, this is presented separately in Figure 13.

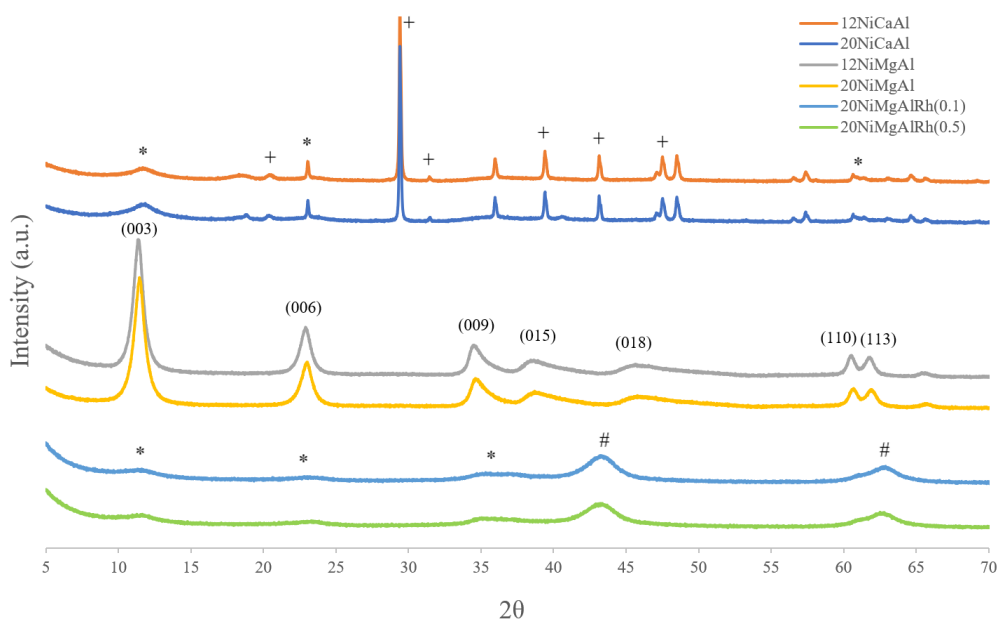


Figure 12: XRD diffraction pattern of HT precursors. \*: hydrotalcite, +:  $\text{CaCO}_3$ , #: MgO

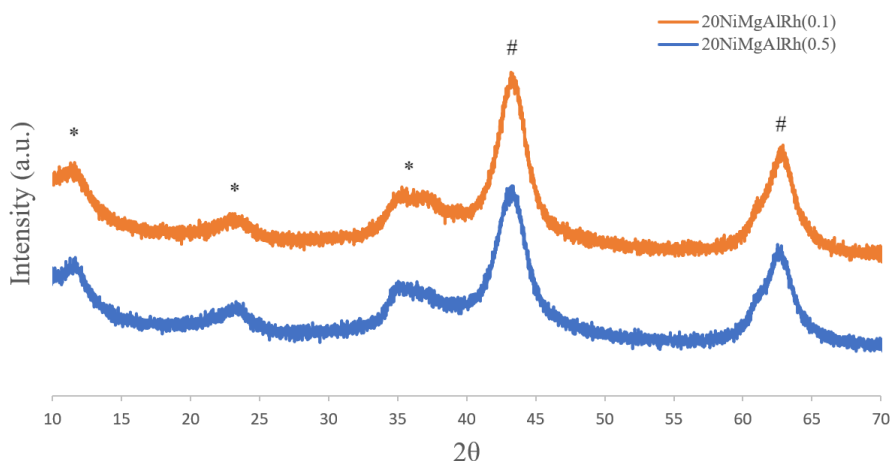


Figure 13: XRD diffraction patterns of the as-prepared rhodium precursors. \*: hydrotalcite, #: MgO

The XRD patterns for NiMgAl precursors show the diffraction pattern that confirms the formation of HTs, with peaks at (003), (006), (009), (015), (018), (110) and (113). The XRD pattern for the NiMgAlRh catalysts show there are some diffraction peaks of HT



structure, indicating that the memory effect has taken place. However, there are also peaks for the MgO phase. The XRD pattern for the NiCaAl precursors show peaks of  $\text{CaCO}_3$ , and only small peaks that correspond to HT structure. This could be because  $\text{CaCO}_3$  is strongly insoluble, and the ionic size of  $\text{Ca}^{2+}$  (0.100 nm) is fairly large compared to  $\text{Mg}^{2+}$  (0.072 nm). [9] [18]

Figure 14 presents the XRD profiles for the calcined catalysts. For the calcined NiMgAl catalysts show it is obvious that the layered structure of HT has been destroyed, and MgO-NiO solids or  $\text{MgAl}_2\text{O}_4/\text{NiAl}_2\text{O}_4$  spinel have been formed. When Ni-Mg-Al ions are used to prepare HTs by co-precipitation, the similar size of these ions leads to that  $\text{Ni}^{2+}$  and  $\text{Al}^{3+}$  can be isomorphically substituted by  $\text{Mg}^{2+}$ . Aluminum is then part of the crystalline structure of the solid HT precursor from substitution with the  $\text{Mg}^{2+}$  ions, and therefore there are no diffraction peaks for  $\text{Al}_2\text{O}_3$ . [22] The XRD pattern for the calcined NiMgAlRh catalysts show that the hydrotalcite structure has been destroyed, and what remains are only the peaks for MgO phase and  $\text{MgAl}_2\text{O}_4 / \text{NiAl}_2\text{O}_4$  spinels. The XRD pattern for calcined NiCaAl catalysts presents clear diffraction peaks for CaO and NiO.

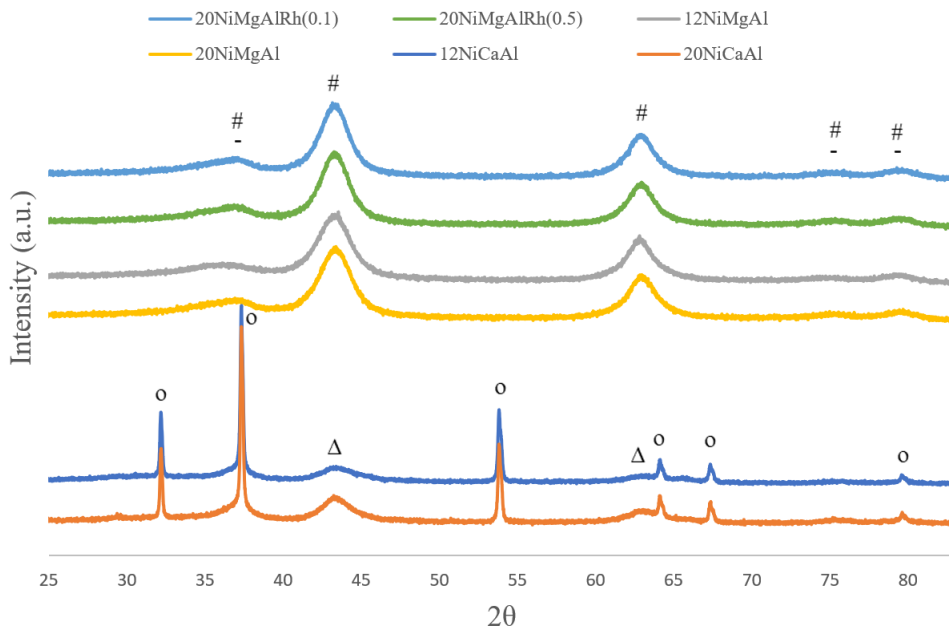


Figure 14: XRD diffraction patterns of calcined catalysts. #: MgO, -:  $\text{MgAl}_2\text{O}_4 / \text{NiAl}_2\text{O}_4$ , o: CaO,  $\Delta$ : NiO

## 4.2 $\text{N}_2$ Physisorption

The  $\text{N}_2$  adsorption/desorption isotherms for the precursor and calcined catalysts are presented in Figures 15 and 18. The pore size distribution for the precursor and calcined catalysts are presented in Figures 16 and 19. To get a clearer view of the pore size distribution of the precursor and calcined NiCaAl catalysts, these are presented apart from the other catalysts in Figures 17 and 20.

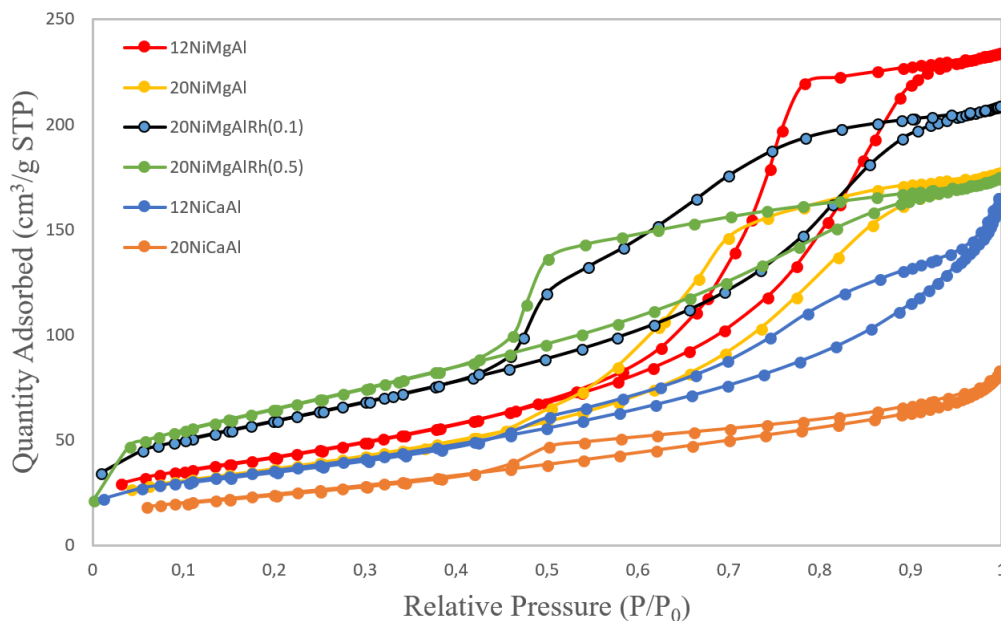


Figure 15: Nitrogen adsorption/desorption isotherms for the precursors

The NiMgAl and NiMgAlRh precursors have a type IV isotherm that indicates they have mesoporous pore structure. The NiCaAl precursor catalysts seem to have type II isotherm, indicating that these two have a macroporous pore structure. The NiMgAl catalysts and 20NiMgAlRh(0.5) catalyst all seem to have H2(b) hysteresis curve, indicating that the pores of the catalyst can have a non-uniform size or shape. The 20NiMgAlRh(0.1) catalysts also resembles a H2(b) hysteresis curve that could have a larger neck width. The 12NiCaAl catalyst show a hysteresis curve that could be of type H3 hysteresis, while 20NiCaAl show a clear type H4 hysteresis curve, suggesting it could consist of solids made up by slit shaped pores, like plates or cubes.

Table 4: Summary of N<sub>2</sub> Physisorption for the HT precursors

Catalyst	Surface Area [m <sup>2</sup> /g]	Pore Volume [cm <sup>3</sup> /g]	Pore Size [nm]
12NiMgAl	153	0.41	7.2
20NiMgAl	132	0.33	5.9
12NiCaAl	129	0.23	6.1
20NiCaAl	89	0.12	4.6

Table 4 summarises the surface area, pore volume and pore size of the HT precursors. For the NiMgAl catalysts, the surface area, pore volume and pore size decreases with increasing percentage in Ni content. This is also the case for the NiCaAl catalysts, which however had much smaller surface areas and pore volumes.

The results for NiMgAlRh catalysts before and after calcination are presented together with the calcined 20NiMgAl catalyst in Table 5 to show how the addition of rhodium affects this catalyst.

Table 5: NiMgAlRh catalysts (precursors and calcined) compared with calcined 20NiMgAl catalyst

Catalyst	Surface Area [m <sup>2</sup> /g]	Pore Volume [cm <sup>3</sup> /g]	Pore Size [nm]
20NiMgAl	205	0.59	8.9
20NiMgAlRh(0.1)	213	0.37	5.2
20NiMgAlRh(0.5)	234	0.29	4.4
20NiMgAlRh(0.1) calc.	202	0.48	5.9
20NiMgAlRh(0.5) calc.	218	0.45	5.2

One can observe that increased addition of rhodium increases the surface area of the 20NiMgAl catalyst, while pore volume and pore size decreases with increasing rhodium added. The reduction in pore size and pore volume of the 20NiMgAl catalyst indicates that the added rhodium are filling the pore space in the 20NiMgAl catalyst. When the NiMgAlRh catalysts are calcined the surface area is decreasing slightly as the layers from the memory effect is destroyed as shown in Figure 14. The pore volume and pore size also increased after calcination. The pore volume are now very equal with 0.48 and 0.45 cm<sup>3</sup>/g for the 20NiMgAlRh(0.1) and NiMgAlRh(0.5), respectively.

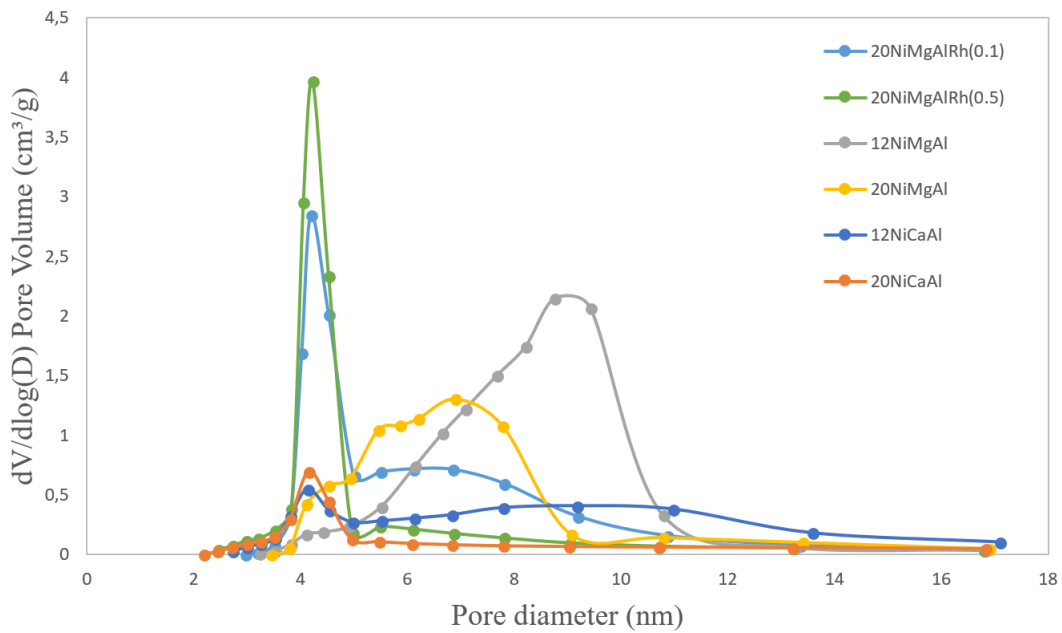


Figure 16: Pore size distribution for the precursors

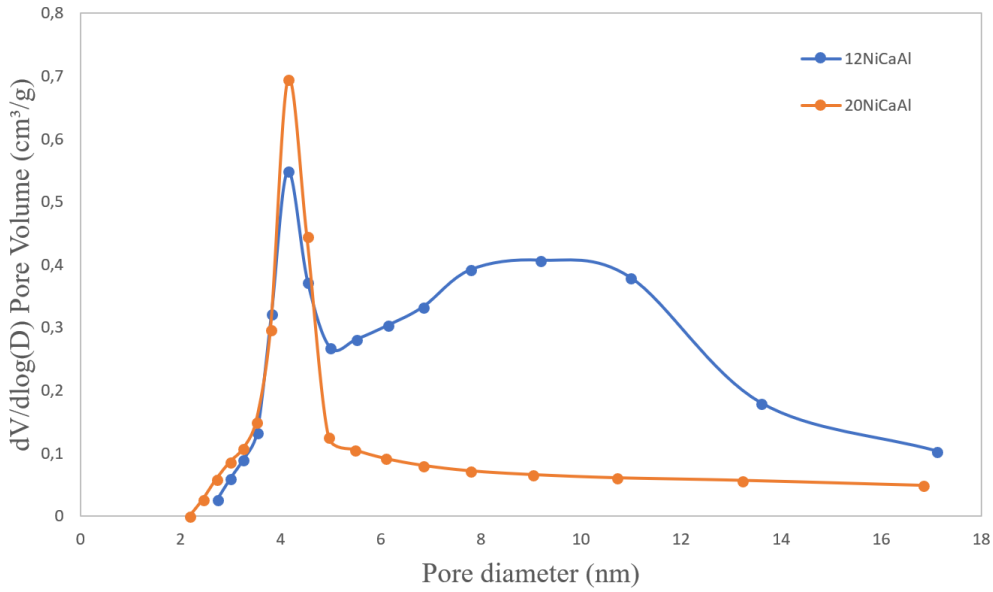


Figure 17: Pore size distribution for the NiCaAl precursors

From Figures 16 and 17 one can observe that the NiMgAlRh catalysts show peaks for pore size distribution at around 4 nm. 12NiMgAl show a pore size distribution between 6-10 nm, with a peak around 9 nm. Figure 17 show a peak at around 4 nm for the 20NiCaAl catalyst. 12NiCaAl also shows a peak at around 4 nm, but also broad peaks between 8-11 nm.

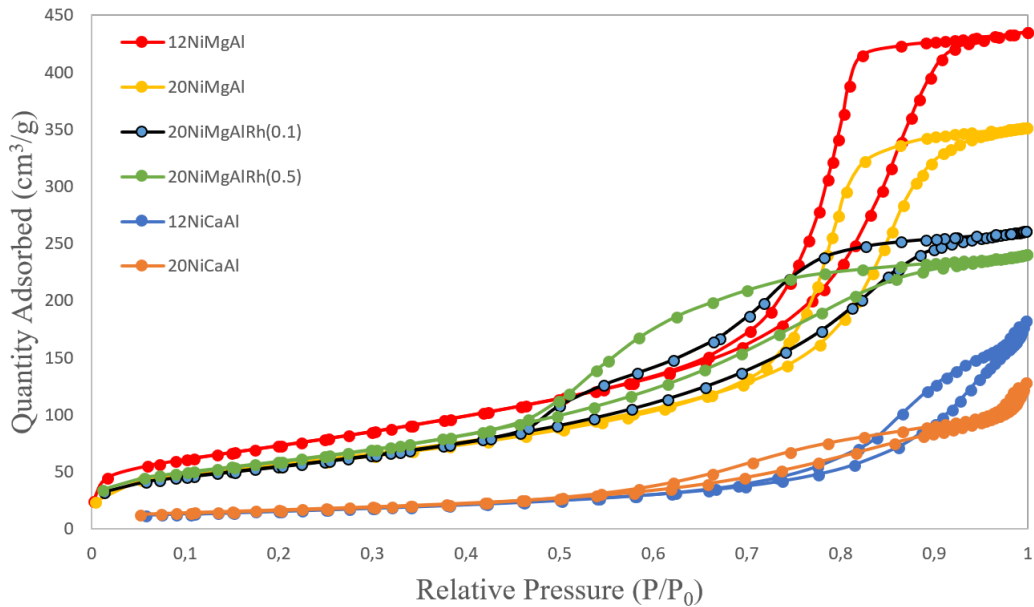


Figure 18: Nitrogen adsorption/desorption isotherms for calcined catalysts

After calcination it looks like all of the calcined catalysts have type IV isotherm curve that indicates they have a mesoporous pore structure. The NiMgAl catalysts appear to have type H2(b) hysteresis form. NiCaAl and NiMgAlRh catalysts show a different type of

H2 hysteresis indicating that the particles have a different structure than for the NiMgAl catalysts.

Table 6: Summary of N<sub>2</sub> Physisorption for the calcined catalysts

Catalyst	Surface Area [m <sup>2</sup> /g]	Pore Volume [cm <sup>3</sup> /g]	Pore Size [nm]
12NiMgAl	268	0.73	8.8
20NiMgAl	205	0.59	8.9
12NiCaAl	58	0.21	10.5
20NiCaAl	61	0.17	7.0
20NiMgAlRh(0.1)	202	0.48	5.9
20NiMgAlRh(0.5)	218	0.45	5.2

The N<sub>2</sub> physisorption for the calcined catalysts are presented in Table 6. It shows that the 12 and 20NiMgAl catalysts have a very high surface area of 268 and 205 m<sup>2</sup>/g, respectively. An interesting observation is that the average pore sizes are almost identical: 8.8 and 8.9 nm. However, the pore volume for 12NiMgAl catalyst are much larger than for 20NiMgAl. The NiCaAl catalysts show very close values for surface area: 58 m<sup>2</sup>/g for 12NiCaAl and 61m<sup>2</sup>/g for 20NiCaAl catalyst. The pore volume are also very close to each other with 0.21 and 0.17 cm<sup>3</sup>/g for 12NiCaAl and 20NiCaAl, respectively. However, there are a large difference in pore size with 10.5 nm for 12NiCaAl, and 7.0 nm for the 20NiCaAl catalyst. It is interesting to see that the surface area for the calcined 20NiMgAlRh(0.1) catalyst are lower than the calcined 20NiMgAl, while the surface area for 20NiMgAlRh(0.5) are slightly higher. Both of the NiMgAlRh catalysts have smaller pore size and pore volume than the 20NiMgAl catalyst.

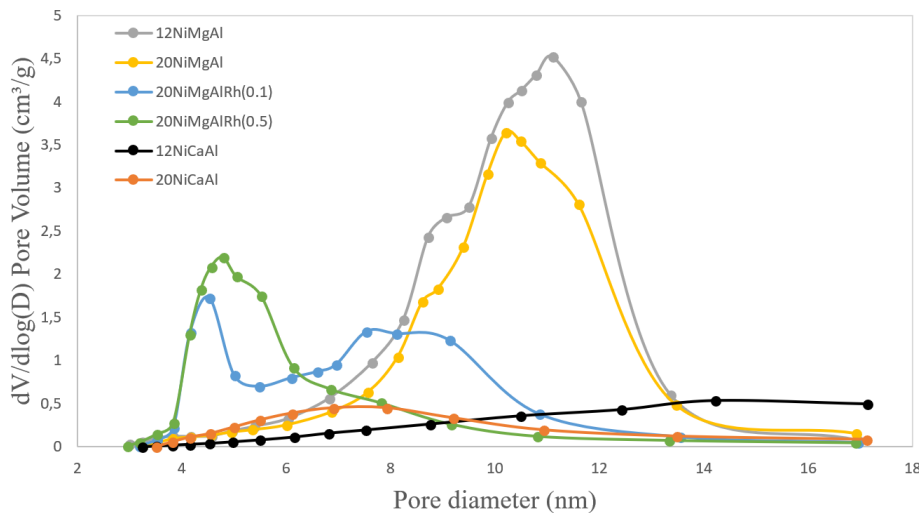


Figure 19: Pore size distribution for calcined catalysts

From Figure 19 the average pore size distribution show a peak around 10 nm and 11 nm for the 12NiMgAl and 20NiMgAl catalysts, respectively. The pore size distribution for 12NiCaAl from Figure 20 show a peak value at around 7 nm, while the 20NiCaAl catalyst

seems to have wide pore size distribution, with a peak at around 14 nm. Pore size distribution for 20NiMgAlRh(0.5) catalyst show a peak at around 5 nm. The 20NiMgAlRh(0.1) catalyst show a peak at around 4.5 nm, but also some peaks between 7-9 nm.

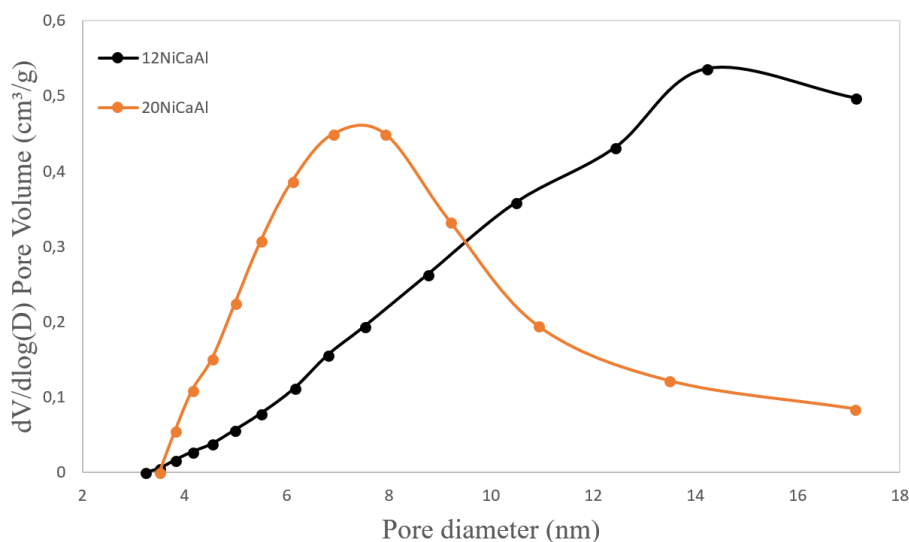


Figure 20: Pore size distribution for calcined NiCaAl catalysts

From the summary of the BET experiment given in Tables 2, 3 and 4, it is observed that for the NiMgAl catalysts there is an increase in surface area, which are one of the improved properties from the calcination of HT. Pore volume and pore size are also increased. For the NiCaAl catalysts the surface area and pore volume decreases. Since the XRD diffraction patterns presented peaks of  $\text{CaCO}_3$  and only weak peaks of HTs, this could suggest that the improved properties for calcined HTs does not go into effect for the NiCaAl catalysts. However, the pore size of these catalysts gets a large increase after calcination. The low surface area and large pore size could lead to greater carbon deposition for the NiCaAl catalysts. When Rh is added to the 20NiMgAl catalyst the surface area increases, while the pore volume and pore size decreases. The surface area increases more on the 0.5 Rh than the 0.1 Rh catalyst, suggesting that increasing wt% of Rh added increases the surface area. The pore volume and pore size decreases with increasing wt% Rh added. The surface area decreases a little after calcination for the NiMgAlRh catalysts, while the pore volume and pore size is increasing. Like the NiCaAl catalysts, the precursors NiMgAlRh catalysts had some diffraction peaks that could be from HT. It would seem that the NiMgAlRh catalysts preserves the properties from calcined HTs better than the NiCaAl catalysts.

### 4.3 TPR

The TPR behavior shows the reduction temperature of the catalysts, and the degree of metal to support interaction [43], which are represented in Figure 21. The 12NiCaAl catalyst have peaks at  $514^\circ\text{C}$  and  $755^\circ\text{C}$ , and the 20NiCaAl catalyst have peaks at  $530^\circ\text{C}$

and 740°C. The peak at the lower temperature are from the reduction of NiO interacting with CaO. The reduction peaks observed at the higher temperatures indicates stronger metal-support interaction between NiO and Al<sub>2</sub>O<sub>3</sub>. [9]

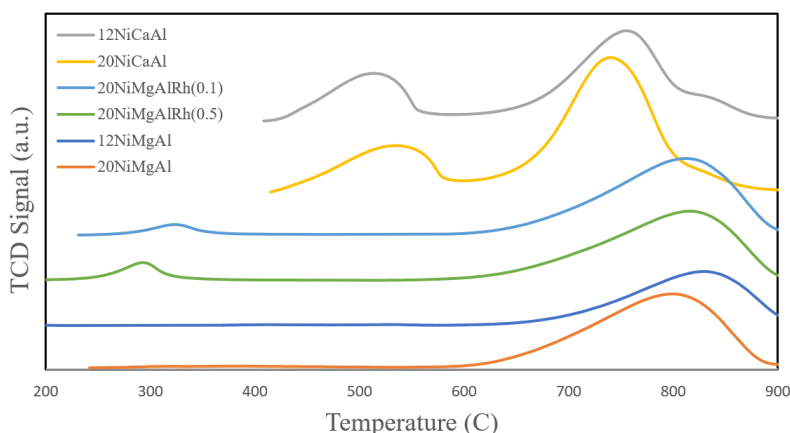


Figure 21: TPR of the catalysts

The TPR profile for the NiMgAl and NiMgAlRh catalysts are very similar, where the two Rh catalysts show small peaks at 323 and 295°C for the NiMgAlRh(0.1) and NiMgAlRh(0.5) catalysts. The high reduction temperatures at 831°C and 798°C for 12NiMgAl and 20NiMgAl, and 814°C for both of the NiMgAlRh catalysts, suggests reduction of Ni<sup>2+</sup> in the solid NiO-MgO solution. The 20NiMgAl catalyst has a peak at lower temperature suggesting that the binding of Ni particles become weaker when the nickel content is higher. [14] [44]

The XRD profile and reduction peaks from TPR for NiMgAl and NiMgAlRh catalysts suggest reduction of metallic Ni in the solid NiO-MgO solution, which corresponds with the XRD diffraction patterns for these catalysts. [22]

#### 4.4 TPD

Temperature programmed desorption are used to determine the basicity at the surface of the different catalysts. It measures the rate of desorption of adsorbed CO<sub>2</sub> molecules as a function of temperature. [39] It is believed that CO<sub>2</sub> adsorption on the weaker basic sites are desorbed at lower temperatures, while CO<sub>2</sub> adsorption on the stronger basic sites are desorbed at higher temperatures. The peak range between 400 and 500°C can be described as medium to strong basic sites for the NiCaAl catalysts. [9] The largest peak are at 462°C for 12NiCaAl, and 459°C for the 20NiCaAl catalyst. The 12NiMgAl and 20NiMgAl catalysts have desorption peaks at 292°C and Mg: 313°C, respectively. For the 12NiMgAL Rh(0.1) and NiMgAlRh(0.5) catalysts, the desorption peaks occur at 299°C and 307°C. As the desorption peaks are in the range of 292-313°C, it suggests that these catalysts desorb CO<sub>2</sub> at weak basic sites. The peaks for the NiCaAl catalysts are higher because CaO adsorbs CO<sub>2</sub> stronger than MgO for the NiMgAl and NiMgAlRh catalysts.

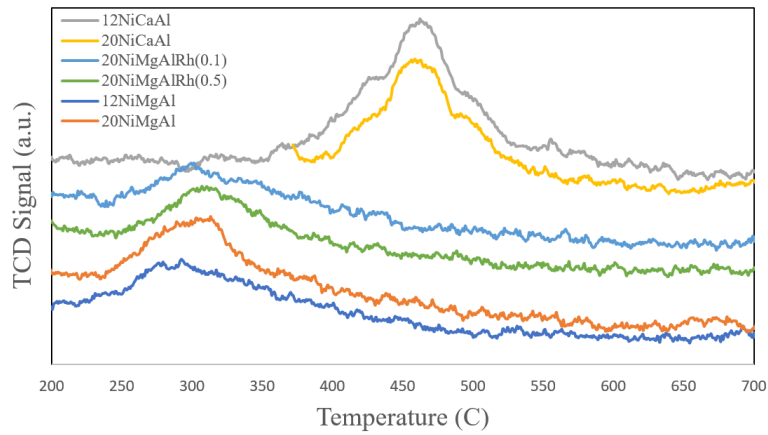


Figure 22: TPD of the catalysts

## 4.5 H<sub>2</sub>-chemisorption

The results from H<sub>2</sub> chemisorption is presented in Table 7. For the NiMgAl and NiCaAl catalysts, higher Ni loading gives higher metal surface area, as would be expected. The calculated dispersion also increases with increased Ni loading, which is explained by that HT derived catalysts do not necessary decrease dispersion by increased loading, as demonstrated by previous study. [42] Addition of 0.1 wt% Rh to the 20NiMgAl catalyst decreases the metal surface area and gives lower dispersion, while the size of the Ni crystals is increasing. The addition of 0.5 wt% of Rh to the 20NiMgAl catalysts increases the metal surface area and dispersion, while the size of the Ni crystals now has decreased slightly.

Table 7: Results from H<sub>2</sub> chemisorption of the catalysts

Catalyst	Metal surface area (m <sup>2</sup> /g <sub>cat</sub> )	Dispersion (%)	Ni crystallite size (nm)
12NiMgAl	2.85	3.56	28.4
20NiMgAl	6.19	4.65	21.8
12NiCaAl	1.42	1.78	57.0
20NiCaAl	3.78	4.74	21.4
20NiMgAlRh(0.1)	5.28	3.95	25.6
20NiMgAlRh(0.5)	6.40	4.73	21.5

## 4.6 DRM reaction

The catalysts were tested at same conditions for the DRM reaction to find out which catalyst would give the best performance according to activity, selectivity and stability. The reactions were run at 750°C and 1 bar for 15 hrs, and at 200 ml/min of a CH<sub>4</sub>/CO<sub>2</sub> feed with molar ratio of 1:1, which gives a GHSV of 240000  $\frac{ml}{g_{cat} \cdot h}$ . Figure 23, 24 and 25 show the CH<sub>4</sub> conversion, CO<sub>2</sub> conversion, and H<sub>2</sub>/CO ratio, respectively.



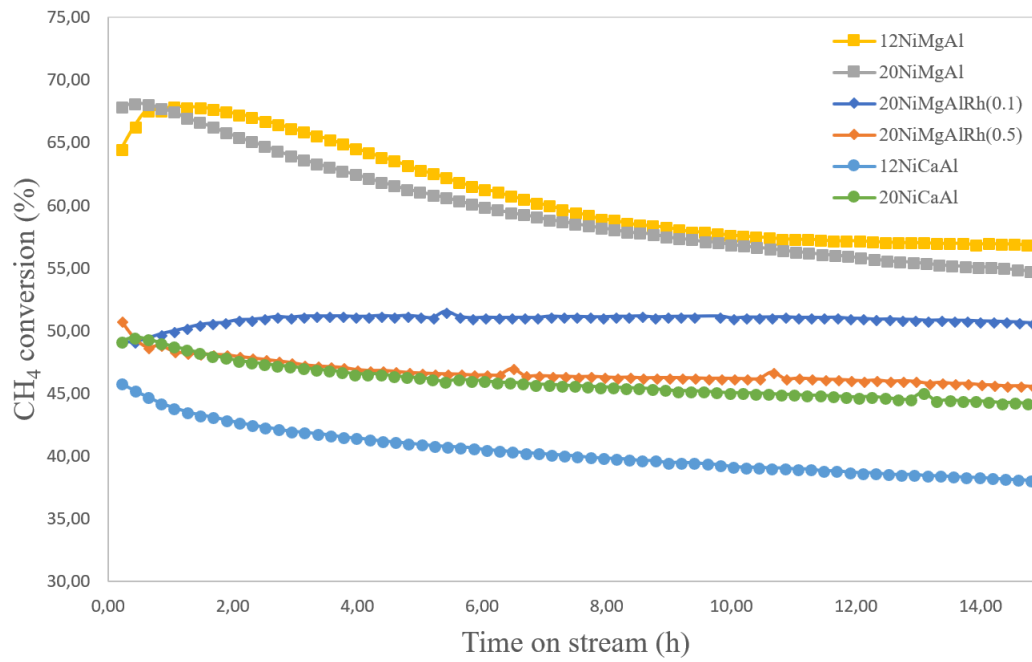


Figure 23: CH<sub>4</sub> conversion for DRM reaction at 750°C and 1 bar

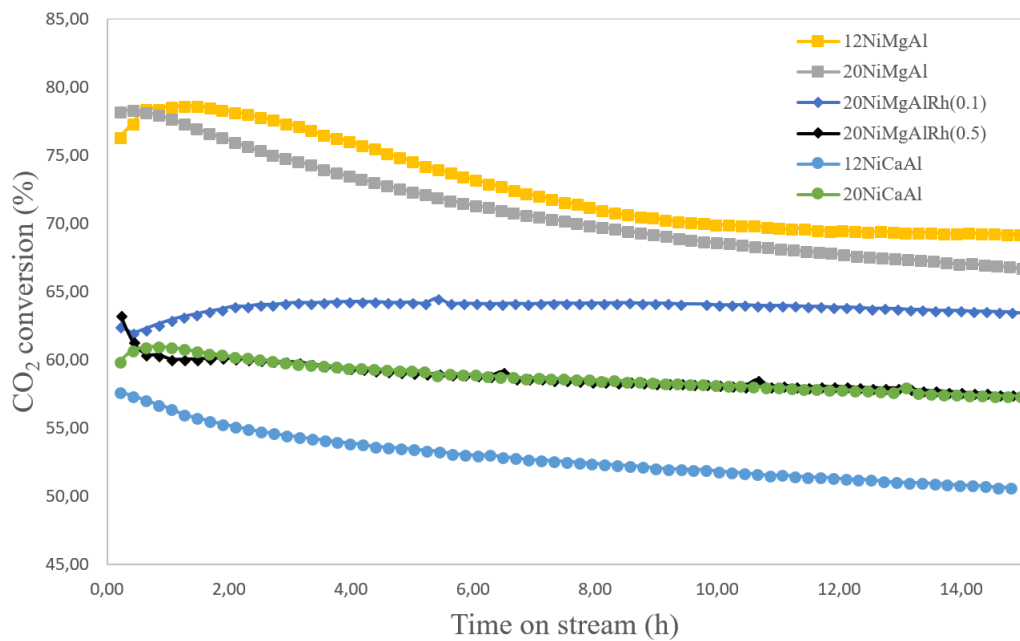


Figure 24: CO<sub>2</sub> conversion for DRM reaction at 750°C and 1 bar

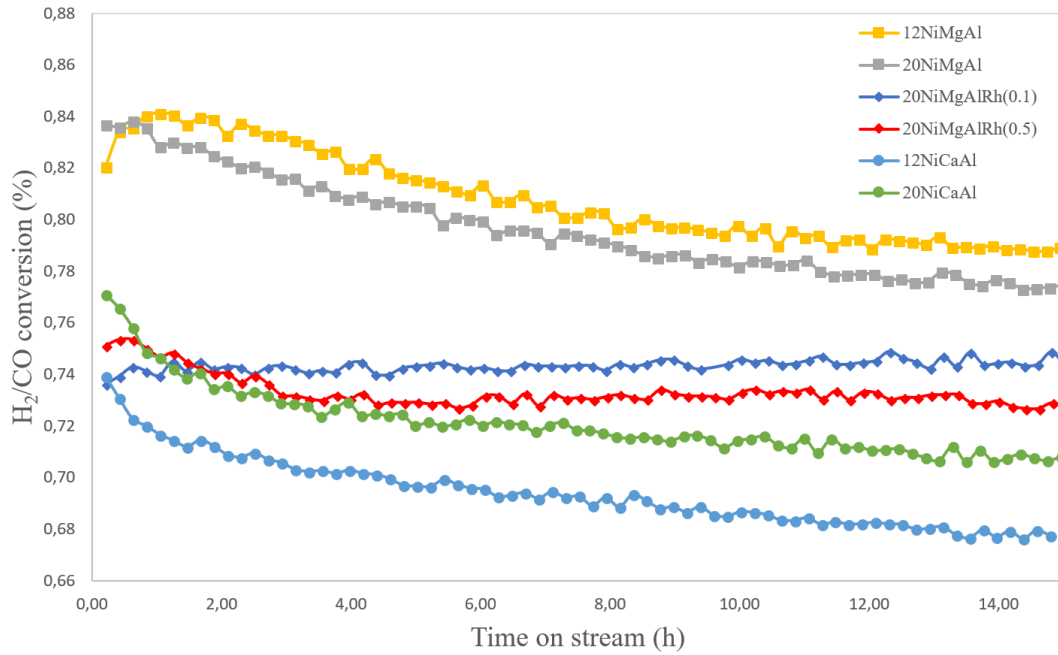


Figure 25: H<sub>2</sub>/CO ratio for DRM reaction at 750°C and 1 bar

The initial and final CH<sub>4</sub> and CO<sub>2</sub> conversion, as well as initial H<sub>2</sub>/CO ratio over 15 h TOS are summarized in Table 8. The CH<sub>4</sub> and CO<sub>2</sub> deactivation from the DRM reaction are represented in Table 9.

Table 8: Results from the DRM reaction

Catalyst	CH <sub>4</sub> <sup>init.</sup>	CH <sub>4</sub> <sup>final</sup>	CO <sub>2</sub> <sup>init.</sup>	CO <sub>2</sub> <sup>final</sup>	H <sub>2</sub> /CO
12NiCaAl	45.8	38.1	57.6	50.7	0.74
20NiCaAl	49.2	44.2	59.9	57.3	0.77
12NiMgAl	64.5	56.9	76.3	69.3	0.82
20NiMgAl	67.9	54.6	78.2	66.6	0.84
20NiMgAlRh(0.1)	49.2	50.2	62.5	62.9	0.74
20NiMgAlRh(0.5)	50.8	45.5	60.4	57.5	0.75

Table 9: CH<sub>4</sub> and CO<sub>2</sub> deactivation from the DRM reaction

Catalyst	CH <sub>4</sub> deactivation (%)	CO <sub>2</sub> deactivation (%)
12NiCaAl	16.8	12.1
20NiCaAl	10.0	4.3
12NiMgAl	11.8	9.2
20NiMgAl	19.6	14.8
20NiMgAlRh(0.1)	-	-
20NiMgAlRh(0.5)	10.5	4.9

CH<sub>4</sub> and CO<sub>2</sub> deactivation are calculated as

$$\text{Deactivation (\%)} = \frac{F_j^{\text{init.}} - F_j^{\text{final}}}{F_j^{\text{init.}}} \cdot 100\% \quad (43)$$

where F represents flow in ml/min at initial and final stages of TOS for DRM reaction. j is CH<sub>4</sub> and CO<sub>2</sub>.

Figure 23 and Table 8 show that the NiMgAl catalysts have the highest initial activity, however after a slight increase they deactivate quite rapidly. The 12NiMgAl catalyst show a tendency to become more stable after 12 hrs TOS. The NiCaAl catalysts do not deactivate so rapidly as the NiMgAl catalysts. This is because CaO adsorbs CO<sub>2</sub> better than MgO, which gasifies deposited carbon. The NiMgAlRh catalysts are the most stable catalysts for CH<sub>4</sub> and CO<sub>2</sub> conversion, due to the addition of Rh. The 20NiMgAl and 12NiCaAl catalysts have the highest CH<sub>4</sub> deactivation with 19.6 and 16.8 %, and highest CO<sub>2</sub> deactivation with 14.8 and 12.1 %, respectively. It is interesting to see that the results from Table 8 show that the 20NiCaAl catalyst are very close to the 20NiMgAlRh(0.5) catalyst. From Table 9 it can be observed that 20NiCaAl have lower CH<sub>4</sub> and CO<sub>2</sub> deactivation than 20NiMgAlRh(0.5). However, Figure 23 show that the NiMgAlRh(0.5) catalyst have a more stable CH<sub>4</sub> conversion for ongoing TOS. The 20NiMgAlRh(0.1) catalyst increases CH<sub>4</sub> and CO<sub>2</sub> conversion and is stable for 15 hrs TOS.

The CO<sub>2</sub> conversion follows the trend of the CH<sub>4</sub> conversion, but have higher values due to the reverse water-gas shift (RWGS) reaction. As for CH<sub>4</sub> conversion, the NiMgAl catalysts have the highest CO<sub>2</sub> conversion followed by the NiMgAlRh catalysts, and the NiCaAl have the lowest CO<sub>2</sub> conversion. The 20NiMgAlRh(0.1) have the most stable CO<sub>2</sub> conversion.

All of the catalysts have a H<sub>2</sub>/CO ratio below 1 which can be explained by the RWGS. Figure 25 shows that the NiMgAlRh catalysts have a stable H<sub>2</sub>/CO ratio, while the NiMgAl and NiCaAl catalysts have a slowly decreasing H<sub>2</sub>/CO ratio.

## 4.7 XRD pattern of the catalysts after DRM reaction

Figure 26 presents the XRD diffraction pattern for the spent catalysts, with the different phases present.

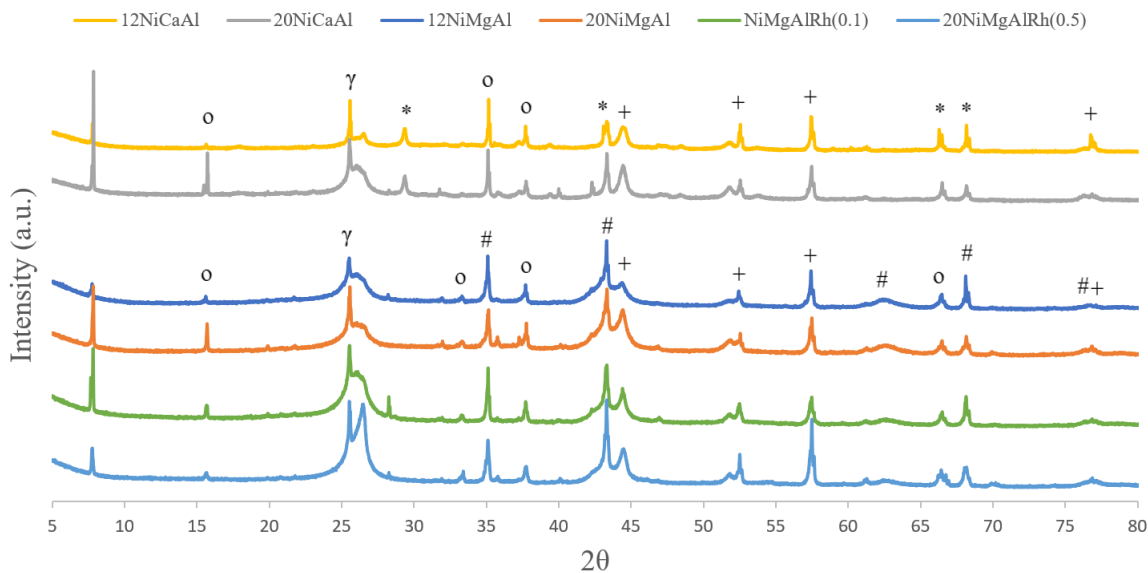


Figure 26: XRD diffraction pattern of spent catalysts after DRM reaction. +: Ni, \*: CaCO<sub>3</sub>, #: MgO, o: MgAl<sub>2</sub>O<sub>4</sub> / NiAl<sub>2</sub>O<sub>4</sub>, γ: graphite

The diffraction patterns indicates that there have been deposited carbon on the catalysts as graphite. For NiCaAl catalysts CaCO<sub>3</sub> and some metallic nickel have been formed. There are also peaks that could be from NiAl<sub>2</sub>O<sub>4</sub> spinel. The NiMgAl and NiMgAlRh catalysts show diffraction peaks of MgO, Ni and MgAl<sub>2</sub>O<sub>4</sub> / NiAl<sub>2</sub>O<sub>4</sub> spinels. There are diffraction peaks at around 7-8° in the diffraction pattern for the spent catalysts, at this stage we are not able to origin of the peak.

## 5 Conclusion

Four different catalysts were prepared by the co-precipitation method. Two NiCaAl and two NiMgAl catalysts with 12 and 20 wt% Ni, respectively. All of the catalysts contained 25 mole % of Al. Two additional catalysts were prepared by adding Rh to the 20NiMgAl catalyst. This created new layers in the catalyst due to the memory effect of HTs. The catalysts were run for DRM reaction to observe the activity and stability of the catalysts. It was discovered that the two NiMgAl catalysts had the highest activity, but also the most rapid deactivation suggesting coke deposition on these catalysts. The NiCaAl catalysts had the lowest activity, but had a stable activity over TOS. The ability that CaO adsorbs CO<sub>2</sub> better than MgO is why the NiCaAl catalysts are more stable than the NiMgAl catalysts. The results for the 20NiCaAl catalyst were similar to the 20NiMgAlRh(0.5) catalyst, but the 20NiMgAlRh(0.5) catalyst was more stable due to that Rh is a noble metal less prone to deactivation. The NiMgAlRh(0.1) catalyst was the most stable catalyst for the DRM reaction.

For future experiments it would be interesting to run tests with a longer TOS and observe how the catalysts will perform. Will the Mg catalysts stabilize, or will they decrease to be below the conversion for the Rh catalysts, and what will happen to the stability of the NiMgAlRh(0.1) catalyst? Also run tests with different composition of feed gas and different temperatures to observe how this affects the catalysts and the results of the DRM reaction.

## References

- [1] D. Phakare, J. Spivey, "A review of dry (CO<sub>2</sub>) reforming of methane over noble metal catalysts", *Chem Soc Review*, Royal Society of Chemistry 2014
- [2] D. J. Wuebbles, K. Hayhoe, "Atmospheric methane and global change", *Earth-Science Reviews* 57 (2002) 177-210
- [3] H. Mahmoudi, M. Mahmoudi, O. Doustdar, H. Jahangiri, A. Tsolakis, S. Gu, M. L. Wyszynski, "A review of Fischer Tropsch synthesis process, mechanism, surface chemistry and catalyst formulation", *Biofuels Eng.* 2017; 2: 11-31
- [4] B. Wang, S. Albarracin-Suazo, Y. Pagan-Torres, E. Nikolla, "Advances in methane conversion processes", *Catalysis Today* 285 (2017) 147-158
- [5] L. Barelli, G. Bidini, F. Gallorini, S. Servili, "Hydrogen production through sorption-enhanced steam methane reforming and membrane technology. A review", *Energy* 33 (2008) 554-570
- [6] A. Kurucz, I. Bendik, "Syngas: Production Methods, Post Treatment and Economics", M. do C. Rangel, M. O. da G. Souza, D. do J. Sodre, A. L. M. da Silva, M. S. Ramos, J. M. Assaf, Chapter 10: Partial Oxidation of Methane over Zirconia-and Magnesia-Supported Ruthenium and Rhodium Catalysts
- [7] M. Z. Nesdah, S. Rowshanzamir, M. H. Eikani, "Autothermal reforming of methane to synthesis gas: Modeling and simulation", *International Journal of Hydrogen Energy* 34 (2009) 1292-1300
- [8] M. A. Reese, S. Q. Turn, H. Cui, "Kinetic modelling of high pressure autothermal reforming", *Journal of Power Sources* 195 (2010) 553-558
- [9] Y. Kathiraser, U. Oemar, E. T. Saw, Z. Li, S. Kawi, "Kinetic and mechanistic aspects for CO<sub>2</sub> reforming of methane over Ni based catalysts", *Chemical Engineering Journal* 278 (2015) 62-78
- [10] J-M Lavoie, "Review on dry reforming of methane, a potentially more environmentally-friendly approach to the increasing natural gas exploitation", *Frontiers in Chemistry* Volume 2 Article 81, November 2014
- [11] N. A. K. Aramouni, J. G. Touma, B. A. Tarboush, J. Zaiter, M. N. Ahmad, "Catalyst design for dry reforming of methane: Analysis review", *Renewable and Sustainable Energy Reviews* 82 (2018) 2570-2585
- [12] J. Ma, N. Sun, X. Zhang, N. Zhao, F. Xiao, W. Wei, Y. Sun, "A short review of catalysis for CO<sub>2</sub> conversion", *Catalysis Today* 148 (2009) 221-231

- [13] O. W. Perez-Lopez, A. Senger, N. R. Marcilio, M. A. Lansarin, "Effect of composition and thermal pretreatment on properties of Ni-Mg-Al catalysts for CO<sub>2</sub> reforming of methane", *Applied Catalysis A: General* 303 (2006) 234-244
- [14] X. Lin, R. Li, M. Lu, C. Chen, D. Li, Y. Zhan, L. Jiang, "Carbon dioxide reforming of methane over Ni catalysts prepared from Ni-Mg-Al layered double hydroxides: influence of Ni loadings", *Fuel* 162 (2015) 271-280
- [15] A. Bhattacharyya, V. W. Chang, D. J. Schumacher, "CO<sub>2</sub> reforming of methane to syngas I: evaluation of hydrotalcite clay-derived catalysts", *Applied Clay Science* 13 (1998) 317-328
- [16] A. Bhattacharyya, US Patent 6 071 433, (2000), BP Amoco Corporation
- [17] R. Debek, M. Motak, T. Grzybek, M. E. Galvez, P. Da Costa, "A short review on the Catalytic Activity of Hydrotalcite-Derived Materials for Dry Reforming of Methane", *Catalysts* 2017, 7, 32
- [18] Z. P. Xu, J. Zhang, M. O. Adebajo, H. Zhang, C. Zhou, "Catalytic applications of layered double hydroxides and derivatives", *Applied Clay Science* 53 (2011) 139-150
- [19] Z. Yu, D. Chen, M. Rønning, T. Vrålstad, E. Ochoea-Fernandez, A. Holmen, "Large-scale synthesis of carbon nanofibers on Ni-Fe-Al hydrotalcite derived catalysts I. Preparation and characterization of the Ni-Fe-Al hydrotalcites and their derived catalysts", *Applied Catalysis A: General* 338 (2008) 136-146
- [20] T. Miyata, D. Li, M. Shiraga, T. Shishido, Y. Oumi, T. Sano, K. Takehira, "Promoting effect of Rh, Pd and Pt noble metals to the Ni/Mg(Al)O catalysts for the DSS-like operation in CH<sub>4</sub> steam reforming", *Applied Catalysis A: General* 310 (2006) 97-104
- [21] F. Teodorescu, A.-M. Paladuta, O. D. Pavel, "Memory effect of hydrotalcites and its impact on cyanoethylation reaction", *Materials Research Bulletin* 48 (2013) 2055-2059
- [22] N. Li, C. Shen, P. Tan, Z. Zao, W. Huang, "Effect of phase transformation on the stability of Ni-Mg-Al catalyst for fry reforming of methane", *Indian Journal of Chemistry* Vol. 54A, October 2015, pp. 1198-1205
- [23] R. Debek, K. Zubek, M. Motak, P. Da Costa, T. Grzybek, "Effect of nickel incorporation into hydrotalcite-based catalysts systems for dry refoming of methane", *Res Chem Intermed* (2015) 41: 9485-9495

- [24] A. C. C. Rodrigues, C. A. Henriques, J. L. F. Monteiro, "Influence of Ni content on Physico-Chemical Characteristics of Ni, Mg, Al-hydrotalcite Like Compounds", *Materials Research*, Vol. 6, No. 4, 563-568, 2003.
- [25] R. Debek, K. Zubek, M. Motak, M. E. Galvez, P. Da Costa, T. Grzybek, "Ni-Al hydrotalcite material as the catalyst precursors for the dry reforming of methane at low temperature", *C. R. Chimie* 18 (2015) 1205-1210
- [26] J. Regalbuto, "Catalyst Preparation: Science and Engineering", CRC Press, Taylor & Francis Group, 2007, pages: 253, 255-257, 344, 378
- [27] I. Chorkendorff, J. W. Niemantsverdriet, "Concepts of Modern Catalysis and Kinetics", WILEY-VCH Verlag GmbH, 2nd Edition 2007: 1st reprint 2011, pages: 143-145, 153-154, 189, 197
- [28] G. Leofanti, M. Padovan, G. Tozzola, B. Venturelli, "Surface area and pore texture of catalysts", *Catalysis Today* 41 (1998) 207-219
- [29] M. Thommes, K. Kaneko, A. V. Neimark, J. P. Oliver, F. Rodriguez-Reinoso, J. Rouquerol, K. S. W. Sing, "Physisorption of gases, with special reference to the evaluation of surface area and pore size distribution (IUPAC Technical Report), *Pure Appl. Chem.* 2015; aop
- [30] K. S. W. Sing, "Reporting Physisorption Data for Gas/Solid Systems", *Pure & Appl. Chem.*, Vol 54, No. 11, pp.2201-2218, 1982.
- [31] Particle Analytical, "Introduction to BET", <http://particle.dk/methods-analytical-laboratory/surface-area-bet-2/>, 20.02.2018
- [32] A.K. Ladavos, A.P. Katsoulidis, A. Iosifidis, K.S. Triantafyllidis, T.J. Pinnavaia, P.J. Pomonis, "The BET equation, the inflection points of N<sub>2</sub> adsorption isotherms and the estimation of specific surface area of porous solids", *Microporous and Mesoporous Materials* 151 (2012) 126-133
- [33] J. Brame and C. Griggs, "Surface Area Analysis Using the Brunauer-Emmett-Teller (BET) Method", ERDC/EL SR-16-3
- [34] K. S. W. Sing, R. T. Williams, "Historical aspects of capillarity and capillary condensation" *Microporous and Mesoporous Materials* 154 (2012) 16-18
- [35] E. Lifshin, "X-ray Characterization of Materials", pages: 4, 24-26, 51-52, 67-68, 72
- [36] G. Ertl, H. Knözinger, J. Weitkamp, "Handbook of Heterogeneous Catalysis", Volume 2 WILEY-VCH 1997, pages: 447, 459-460, 676-677



- [37] P. A. Webb, "Introduction to Chemical Adsorption Analytical Techniques and their Applications to Catalysis", MIC Technical Publications January 2003
- [38] J. W. Niemantsverdriet, "Spectroscopy in Catalysis: An Introduction", WILEY-VCH Verlag GmbH & co, 2007, pages: 11-12, 19-20, 180-185
- [39] A. Auroux, "Calorimetry and Thermal Methods in Catalysis", Springer Series in Material Science, Volume 154. pages: 133, 139-142, 185-186
- [40] M. A. Reiche, M. Maciejewski, A. Baiker, "Characterization by temperature programmed reduction", Catalysis Today 56 (2000) 347-355
- [41] M. Che, J. C. Védrine, "Characterization of Solid Materials and Heterogeneous Catalysts: From Structure to Surface Reactivity", Volume 2, WILEY-VCH, pages: 863-865
- [42] D. Y. Kalai, K. Stangeland, Y. Jin, Z. Yu, "Active and stable hydrotalcite derived Ni catalysts for CO<sub>2</sub> reforming of methane: Comparison with catalysis by incipient wetness", Journal of CO<sub>2</sub> Utilization (2017)
- [43] K. Y. Koo, H-S Roh, Y. T. Seo, D. J. Seo, W. L. Yoon, S. B. Park, "A highly effective and stable nano-sized Ni/MgO-Al<sub>2</sub>O<sub>3</sub> catalyst for gas to liquids (GTL) process", International Journal of Hydrogen Energy 33 (2008) 2036-2043
- [44] D. Li, L. Wang, M. Koike, Y. Nakagawa, K. Tomishige, "Steam reforming of tar from pyrolysis of biomass over Ni/Mg/Al catalysts prepared from hydrotalcite-like precursors", Applied Catalysis B: Environmental 102 (2011) 528-538

## A Calculations used in the thesis

### A.1 Summary of precursor calculation

To calculate the stoichiometric amounts of cations and anions needed for co-precipitation of the catalysts, the following equations were used. In the example  $a = \text{Ni}$ ,  $b = \text{Mg}$ ,  $c = \text{Al}$  and  $d = \text{Ca}$

$$x = \frac{M^{3+}}{M_y^{2+} + M_z^{2+} + M^{3+}} = \frac{c}{a + b + c} = 0.25 \quad (44)$$

From (44)

$$a + b + c = 1 \quad \text{and} \quad c = 0.25 \Rightarrow \quad (45)$$

$$a + b = 0.75 \Rightarrow a = 0.75 - b \quad (46)$$

For Mg with 12 wt% Ni

$$\text{wt}\% = \frac{aM_{\text{Ni}}}{aM_{\text{Ni}} + bM_{\text{MgO}} + \frac{c}{2}M_{\text{Al}_2\text{O}_3}} = 0.12 \quad (47)$$

Inserting equation (44) and (46) into (47) and solve for  $b$  gives a final equation for how much of moles initially needed to get the right stoichiometric relationships for the solutions. (the intermediate calculation steps are not shown here).

$$\text{For 0.12 Mg catalyst: } b = \frac{-0.66M_{\text{Ni}} + 0.015M_{\text{Al}_2\text{O}_3}}{-0.88M_{\text{Ni}} - 0.12M_{\text{MgO}}}$$

$$\text{For 0.2 Mg catalyst: } b = \frac{-0.6M_{\text{Ni}} + 0.025M_{\text{Al}_2\text{O}_3}}{-0.8M_{\text{Ni}} - 0.2M_{\text{MgO}}}$$

$$\text{For 0.12 Ca catalyst: } d = \frac{-0.66M_{\text{Ni}} + 0.015M_{\text{Al}_2\text{O}_3}}{-0.88M_{\text{Ni}} - 0.12M_{\text{CaO}}}$$

$$\text{For 0.2 Ca catalyst: } d = \frac{-0.6M_{\text{Ni}} + 0.025M_{\text{Al}_2\text{O}_3}}{-0.8M_{\text{Ni}} - 0.2M_{\text{CaO}}}$$

The initial moles for the cations and anions needed for calculation of mass for each of the different salts are presented in Tables 10 and 11

Table 10: Initial moles for mass calculation for Mg catalysts

wt%	a Ni <sup>2+</sup>	b Mg <sup>2+</sup>	c Al <sup>3+</sup>	CO <sub>3</sub> <sup>2-</sup>	OH <sup>-</sup>
0.12	0.091	0.659	0.25	0.125	2
0.2	0.156	0.594	0.25	0.125	2

Table 11: Initial moles for mass calculation for Ca catalysts

wt%	a Ni <sup>2+</sup>	d Ca <sup>2+</sup>	c Al <sup>3+</sup>	CO <sub>3</sub> <sup>2-</sup>	OH <sup>-</sup>
0.12	0.113	0.637	0.25	0.125	2
0.2	0.188	0.562	0.25	0.125	2

The total volume of the combined solution of cations and anions was set to contain 0.8 L. To get good precipitation, the concentration of the total M<sup>2+</sup> and M<sup>3+</sup> was set to 0.5 M (mol/liter) The volume of the first solution was 0.4 L, giving a total amount of 0.2 moles for each component in this solution. To avoid pillaring in the catalyst, the content of Na<sub>2</sub>CO<sub>3</sub> has an excess value of moles equal to 0.4. This gives the moles needed for mass calculation of the Mg and Ca catalysts, presented in Tables 12 and 13

Table 12: Moles for mass calculation of Mg catalysts

wt%	a Ni <sup>2+</sup>	b Mg <sup>2+</sup>	c Al <sup>3+</sup>	CO <sub>3</sub> <sup>2-</sup>	OH <sup>-</sup>
0.12	0.018	0.132	0.05	0.05	0.4
0.2	0.031	0.119	0.05	0.05	0.4

Table 13: Moles for mass calculation of Ca catalysts

wt%	a Ni <sup>2+</sup>	d Ca <sup>2+</sup>	c Al <sup>3+</sup>	CO <sub>3</sub> <sup>2-</sup>	OH <sup>-</sup>
0.12	0.023	0.127	0.05	0.05	0.4
0.2	0.038	0.112	0.05	0.05	0.4

Tables 14 and 15 represents the mass of the salts used in the co-precipitation of the precursors

Table 14: Mass of the salts used for co-precipitation of Mg catalysts

	Ni(NO <sub>3</sub> ) <sub>2</sub> · 6 H <sub>2</sub> O	Mg(NO <sub>3</sub> ) <sub>2</sub> · 6 H <sub>2</sub> O	Al(NO <sub>3</sub> ) <sub>3</sub> · 9 H <sub>2</sub> O	Na <sub>2</sub> (CO) <sub>3</sub>	NaOH
molar mass	290.81	256.41	375.13	105.99	40
mass (0.12)	5.3105	33.7792	18.7565	5.2995	16
mass (0.2)	9.0873	30.4491	18.7565	5.2995	16

Table 15: Mass of the salts used for co-precipitation of Ca catalysts

	Ni(NO <sub>3</sub> ) <sub>2</sub> · 6 H <sub>2</sub> O	Ca(NO <sub>3</sub> ) <sub>2</sub> · 4 H <sub>2</sub> O	Al(NO <sub>3</sub> ) <sub>3</sub> · 9 H <sub>2</sub> O	Na <sub>2</sub> (CO) <sub>3</sub>	NaOH
molar mass	290.81	236.15	375.13	105.99	40
mass (0.12)	6.5524	30.1017	18.7565	5.2995	16
mass (0.2)	10.9599	26.5226	18.7565	5.2995	16

## A.2 Addition of rhodium to 20NiMgAl catalyst

The wt% of rhodium that are calculated as

$$\frac{m_{Rh}}{m_{Rh} + m_{cat}} = x \Rightarrow \quad (48)$$

$$m_{Rh} = x \cdot [m_{Rh} + m_{cat}] \Rightarrow \quad (49)$$

$$m_{Rh}(1 - x) = x \cdot m_{cat} \Rightarrow \quad (50)$$

$$\boxed{m_{Rh} = \frac{x \cdot m_{cat}}{1 - x}} \quad (51)$$

which gives the final equation for mass of rhodium, where  $x$  is wt % and  $m_{cat}$  is the amount of mass of the 0.2 Mg catalyst.

To find the required mass of the rhodium-salt for the experiment, another equation is needed

$$\frac{m_{Rh}}{m_{Rh-salt}} = \frac{M_{Rh}}{M_{Rh-salt}} \quad (52)$$

M: molecular weight

m: mass weight

We need to find the mass of the Rh-salt. From equation (52)

$$m_{Rh-salt} = m_{Rh} \cdot \frac{M_{Rh-salt}}{M_{Rh}} \quad (53)$$

$M_{Rh-salt} = 288.92$  g/mol and  $M_{Rh} = 102.91$  g/mol

The summary of the different constants used are displayed in Table 16

Table 16: Summary of IW method for the prepared Rh catalysts

Catalyst	wt% Rh	$m_{cat}$ (g)	$m_{Rh}$ (g)	$m_{Rh-salt}$ (g)
NiMgAlRh(0.1)	0.1	2.7931	0.0028	0.0078
NiMgAlRh(0.5)	0.5	2.6745	0.0134	0.0377

## B Calculation of mass for TPR experiment based on the sensitivity and resolution factor

To get good results for the TPR experiment, the sensitivity factor,  $K$ , and resolution factor,  $P$ , must be within a certain range. This is determined from the the equations

$$K = \frac{S^\circ}{V \cdot C^\circ} \quad (54)$$

$$P = \beta \cdot K \quad (55)$$

where  $55 \leq K \leq 140$  and  $P \leq 20$ .

$S^\circ [\mu\text{mol}]$  is the initial amount of reducible species in the sample.  $V$  is the total flow rate [ $\text{cm}^3/\text{s}$ ] and  $C^\circ$  is the hydrogen concentration in the carrier gas [ $\mu\text{mol}/\text{cm}^3$ ].  $\beta$  is the heat rate used in the experiment.

To find the amount of reducible species in the sample, we need the moles of the cations used for mass calculation and the molar mass of the oxides. This is presented in Tables 17 and 18

Table 17: Moles of cations for the Mg catalysts

wt%	a Ni <sup>2+</sup>	b Mg <sup>2+</sup>	c Al <sup>3+</sup>
0.12	0.018	0.132	0.05
0.2	0.031	0.119	0.05

Table 18: Moles of cations for the Ca catalysts

wt%	a Ni <sup>2+</sup>	d Ca <sup>2+</sup>	c Al <sup>3+</sup>
0.12	0.023	0.127	0.05
0.2	0.038	0.112	0.05

The molar mass of the oxides are presented in Table 19

Table 19: Molar mass of oxides

Symbol	M (g/mol)
MgO	40.31
CaO	56.08
Al <sub>2</sub> O <sub>3</sub>	101.96
NiO	74.69

To calculate the reducible amount ( $\mu\text{mol/g}$ ) we need the  $\text{mmol/g}$  calcined catalyst. The example presented in equation (56) is the calculation for the two NiMgAl catalysts.

$$\frac{aM_{Ni} \cdot 1000}{aM_{Ni} + bM_{MgO} + \frac{c}{2}M_{Al_2O_3}} \quad (56)$$

This value is then multiplied with the mass of the sample to get the value for the reducible amount  $\mu\text{mol}$  for the sample

For TPR we have set the heating rate to  $10^\circ\text{C}/\text{min} = 0.167^\circ\text{C}/\text{s}$ .  $\text{H}_2$  flow (V) is  $50 \text{ cm}^3/\text{min} = 0.83 \text{ cm}^3/\text{s}$ , and  $\text{H}_2$ -concentration is 10%. The standard volume for 1 mole of ideal gas is  $22414 \text{ cm}^3$ , so we have  $4.4615 \cdot 10^{-5} \text{ mol}/\text{cm}^3$ , which is  $44.615 \mu\text{mol}/\text{cm}^3$ . Since the concentration of  $\text{H}_2$  is 10%, we get the value for  $C^\circ$  to be  $4.4615 \mu\text{mol}/\text{cm}^3$ .

Table 20 show that we get good ranges for  $K$  and  $P$  for all the catalysts when about 0.1225 g of sample is being used in TPR.

Table 20: Summary of calculations for  $K$  and  $P$

Catalyst	Mass of sample used (g)	mmol/g calcined	reducible amount ( $\mu\text{mol}$ )	$K$	$P$
0.12 Mg	0.1226	1.98	242.73	65.29	10.88
0.2 Mg	0.1225	3.23	395.86	106.47	17.75
0.12 Ca	0.1225	1.98	242.53	65.23	10.87
0.2 Ca	0.1227	3.23	396.51	106.65	17.77
0.1 Rh	0.1229	1.98	243.33	65.45	10.91
0.5 Rh	0.1222	3.23	394.89	106.21	17.70